

UCLA

UCLA Previously Published Works

Title

Dissolution susceptibility of glass-like carbon versus crystalline graphite in high-pressure aqueous fluids and implications for the behavior of organic matter in subduction zones

Permalink

<https://escholarship.org/uc/item/4zi5m0v2>

Authors

Tumiati, Simone
Tiraboschi, Carla
Miozzi, Francesca
et al.

Publication Date

2020-03-01

DOI

10.1016/j.gca.2020.01.030

Peer reviewed

Dear author,

Please note that changes made in the online proofing system will be added to the article before publication but are not reflected in this PDF.

We also ask that this file not be used for submitting corrections.



Dissolution susceptibility of glass-like carbon versus crystalline graphite in high-pressure aqueous fluids and implications for the behavior of organic matter in subduction zones

Simone Tumiatì^{a,*}, Carla Tiraboschi^{a,b}, Francesca Miozzi^{a,c},
Alberto Vitale-Brovarone^{c,d}, Craig E. Manning^e, Dimitri Sverjensky^f,
Sula Milani^a, Stefano Poli^a

^a Dipartimento di Scienze della Terra, Università degli Studi di Milano, via Mangiagalli 34, 20133 Milano, Italy

^b Institut für Mineralogie, Universität Münster, Correnstrasse 24, 48149 Münster, Germany

^c Sorbonne Université, Muséum National d'Histoire Naturelle, UMR CNRS 7590, IRD, Institut de Minéralogie, de Physique des Matériaux et de Cosmochimie, IMPMC, 75005 Paris, France

^d Dipartimento di Scienze della Terra, Università degli Studi di Torino, via Valperga Caluso 35, 10125 Torino, Italy

^e Department of Earth, Planetary and Space Sciences, University of California, Los Angeles, CA 90095-1567, USA

^f Department of Earth & Planetary Sciences, Johns Hopkins University, Baltimore, MD 21218, USA

Received 12 July 2019; accepted in revised form 15 January 2020; available online xxxx

Abstract

Organic matter, showing variable degrees of crystallinity and thus of graphitization, is an important source of carbon in subducted sediments, as demonstrated by the isotopic signatures of deep and ultra-deep diamonds and volcanic emissions in arc settings. In this experimental study, we investigated the dissolution of sp^2 hybridized carbon in aqueous fluids at 1 and 3 GPa, and 800 °C, taking as end-members (i) crystalline synthetic graphite and (ii) X-ray amorphous glass-like carbon. We chose glass-like carbon as an analogue of natural “disordered” graphitic carbon derived from organic matter, because unlike other forms of poorly ordered carbon it does not undergo any structural modification at the investigated experimental conditions, allowing approach to thermodynamic equilibrium. Textural observations, Raman spectroscopy, synchrotron X-ray diffraction and dissolution susceptibility of char produced by thermal decomposition of glucose (representative of non-transformed organic matter) at the same experimental conditions support this assumption. The redox state of the experiments was buffered at $\Delta FMQ \approx -0.5$ using double capsules and either fayalite-magnetite-quartz (FMQ) or nickel-nickel oxide (NNO) buffers. At the investigated P – T – fO_2 conditions, the dominant aqueous dissolution product is carbon dioxide, formed by oxidation of solid carbon. At 1 GPa and 800 °C, oxidative dissolution of glass-like carbon produces 16–19 mol% more carbon dioxide than crystalline graphite. In contrast, fluids interacting with glass-like carbon at the higher pressure of 3 GPa show only a limited increase in CO_2 (fH_2^{NNO}) or even a lower CO_2 content (fH_2^{FMQ}) with respect to fluids interacting with crystalline graphite. The measured fluid compositions allowed retrieving the difference in Gibbs free energy (ΔG) between glass-like carbon and graphite, which is +1.7(1) kJ/mol at 1 GPa–800 °C and +0.51(1) kJ/mol (fH_2^{NNO}) at 3 GPa–800 °C. Thermodynamic modeling suggests that the decline in dissolution susceptibility at high pressure is related to the higher compressibility of glass-like carbon with respect to crystalline graphite, resulting in G – P curves crossing at about 3.4 GPa at 800 °C, close to the graphite–diamond transition. The new experimental data suggest that, in the presence of aqueous fluids that

* Corresponding author.

E-mail address: simone.tumiati@unimi.it (S. Tumiatì).

flush subducted sediments, the removal of poorly crystalline “disordered” graphitic carbon is more efficient than that of crystalline graphite especially at shallow levels of subduction zones, where the difference in free energy is higher and the availability of poorly organized metastable carbonaceous matter and of aqueous fluids produced by devolatilization of the downgoing slab is maximized. At depths greater than 110 km, the small differences in ΔG imply that there is minimal energetic drive for transforming “disordered” graphitic carbon to ordered graphite; “disordered” graphitic carbon could even be energetically slightly favored in a narrow P interval.

© 2020 Elsevier Ltd. All rights reserved.

1. INTRODUCTION

The carbon isotopic signature of the upper mantle, transition zone and lower mantle (Stachel et al., 2002; Cartigny et al., 2004; Palot et al., 2014), and of gaseous CO_2 emitted from arc volcanoes (Mason et al., 2017) suggests that organic matter subducted within sediments displays a major role in the deep carbon cycle (Hayes and Waldbauer, 2006). The dissolution of graphitic carbon in aqueous fluids due to oxidation or reduction processes (Connolly and Cesare, 1993; Connolly, 1995; Zhang et al., 2018; Tumiati and Malaspina, 2019) is of primary importance as it governs the removal of organic matter from the sediments flushed by fluids released from the dehydrating subducted plate (Schmidt and Poli, 2013). In contrast to carbonates (e.g., Kelemen and Manning, 2015), graphite has long been considered to represent a refractory sink of carbon in the subducting slab (Plank and Manning, 2019), showing low solubility in metamorphic fluids (Connolly and Cesare, 1993) and silicate melts (Duncan and Dasgupta, 2017). However, recent thermodynamic models and experiments suggest that graphite can be readily dissolved in subduction fluids (Manning et al., 2013), stressing for instance the importance of pH (Sverjensky et al., 2014a,b) and of dissolved silica (Tumiati et al., 2017). However, it is still not known how graphite crystallinity might affect the compositions of COH fluids in subduction zones.

Carbonaceous material in sedimentary rocks metamorphosed under temperature and pressure conditions characteristic of subduction zones exhibit a progressive increase in crystallinity (e.g., Beyssac et al., 2002). Besides exceptional preservations of amorphous-like carbon in some metamorphic rocks (Bernard et al., 2007), carbonaceous material metamorphosed under prograde temperature increase to about 550 °C is characterized by a variety of turbostratic structures, from poorly crystallized to almost crystalline, that are commonly referred to as disordered graphitic C (Beyssac and Rumble, 2014; Vitale Brovarone et al., 2013; Bollinger et al., 2004)). Carbonaceous material in high-temperature and ultra-high-pressure terranes is instead characterized by rather crystalline graphite (Beyssac et al., 2002). Thus, disordered graphitic carbon should represent the most common form of carbonaceous material under forearc to sub-arc metamorphic conditions where large amounts of aqueous fluids are released from the slab.

Crystalline (ordered) graphite is crystallographically defined by an interplanar d value of exactly 3.35 Å and a long-range crystalline order with crystallite size of at least a few dozen nanometers (Luque et al., 1998). The chemical

bonds within the layers of hexagonally arranged carbon atoms are covalent with sp^2 hybridization (Fitzer et al., 1995; Langenhorst and Campione, 2019). The thermodynamic properties of carbon without long-range crystalline order and of poorly crystallized and/or defect-rich (“disordered”) graphitic carbon are not available at high-pressure and high-temperature conditions, hence thermodynamic models generally assume perfect ordering and well-developed crystallinity of graphite. Although some studies suggested that “disordered” graphite and well crystallized graphite may display different dissolution behavior in aqueous fluids (Ziegenbein and Johannes, 1980; Connolly, 1995; Luque et al., 1998), others concluded that their thermodynamic properties must be very similar (McCullom, 2013).

In this study, we provide the first experimental results on the high-pressure/high-temperature dissolution at relatively oxidized conditions of i) ordered crystalline graphite (with crystallite size around 50 nm determined by synchrotron X-ray diffraction and small Raman “disorder” D peak) and ii) X-ray amorphous glass-like carbon, by measuring the CO_2 content of aqueous fluids in equilibrium with these two sp^2 -hybridized carbon forms. Glass-like carbon is indeed a typical disordered sp^2 bonded carbon (like graphitic carbon) consisting of randomly distributed curved graphene layer (also called disordered multilayer graphene, or DMLG) fragments dispersed in an amorphous matrix (Hu et al., 2017). Glass-like carbon is non-crystalline (X-ray amorphous) and non-graphitizing, meaning that it resists the development of graphite crystals up to 3000 °C at room pressure, and up to 45 GPa at room temperature (Shiell et al., 2018). From a thermodynamic point of view, glass-like carbon can be considered as a quasi-amorphous or crypto-crystalline solid with crystallite dimensions smaller than 5–8 nm (Guencheva et al., 2001). In light of these properties, we used glass-like carbon as an analogue of poorly organized organic matter. The advantage of using glass-like carbon instead of other poorly crystalline disordered carbon allotropes lies in its metastable persistence at the investigated experimental conditions (1–3 GPa, 800 °C, 12–24 h). Other disordered carbon materials, such as saccharose-based char, are known to recrystallize promptly at high-pressure/high-temperature conditions (Beyssac et al., 2003), which would prevent equilibration between fluids and solid carbon in days-long runs, and therefore the retrieval of thermodynamic parameters. The choice of using glass-like carbon as an analogue for natural disordered carbon is also supported by comparison of glass-like carbon with char produced by thermal decomposition of glucose at the same experimental conditions.

The experimental results allowed retrieving the difference in Gibbs free energy (G) of glass-like carbon compared to that of crystalline graphite at high pressures and temperatures, demonstrating that, although small, this difference can lead to substantial changes in dissolved carbon content predicted by available thermodynamic models that assume a perfectly ordered crystalline state of graphitic carbon.

2. METHODS

In this study, we use the recommended terminology of IUPAC (Fitzer et al., 1995) for the description of carbon as a solid, which is summarized in the Appendix.

2.1. Bulk compositions, starting materials and buffering strategy

Fluids in equilibrium with crystalline and disordered sp^2 carbon were generated starting from oxalic acid dihydrate (OAD; $H_2C_2O_4 \cdot 2H_2O$; Sigma-Aldrich), highly ordered graphite powder (from spectroscopic-pure rods, gently hand-ground in boron carbide mortar) and glass-like carbon spherical powder (Alfa Aesar; type I, i.e., produced by firing polymeric precursors at temperatures below 2000 °C). Crystalline graphite and glass-like carbon were characterized by scanning-electron microscopy, micro-Raman spectroscopy and synchrotron X-ray diffraction. Additionally, two experiments have been replicated using pure water (MilliQ, boiled while flushed with N_2 to remove dissolved atmospheric CO_2) instead of OAD to check for possible discrepancies. Experiments were buffered using the double-capsule technique (Eugster and Skippen, 1967) to prevent the direct contact with the buffering assemblages, with an inner H_2 -permeable $Au_{60}Pd_{40}$ capsule (OD = 2.3 mm) and an outer Au capsule (OD = 4.5 mm). The outer capsule contained H_2O and either the fayalite–magnetite–quartz (FMQ) or the nickel–nickel oxide (NNO) buffers (Fig. 1). Fayalite and magnetite have been synthesized at 1100 °C in a gas-mixing furnace under reducing atmosphere (CO_2 : $CO = 10:1$), starting from stoichiometrically weighted reagent-grade Fe_2O_3 (Sigma-Aldrich) and amorphous SiO_2 from hydrolyzed tetraethyl orthosilicate (Sigma-Aldrich). Natural hyaline quartz powder has been used to build up the final FMQ buffering assemblage. NNO buffer was prepared by mixing Ni metal powder (Sigma-Aldrich) and green NiO nanopowder (Sigma-Aldrich), previously sintered at 1300 °C for 24 h under oxidizing atmosphere to prevent grain size-induced discrepancies with the accepted free-energy values of the NNO buffer (Mattioli and Wood, 1988; O'Neill and Pownceby, 1993). At equilibrium conditions, as long as all the buffering phases are present, the chemical potential of hydrogen is expected to be homogeneous in the inner and in the outer capsules. In the outer capsule, the hydrogen fugacity (fH_2) is constrained through the reactions:

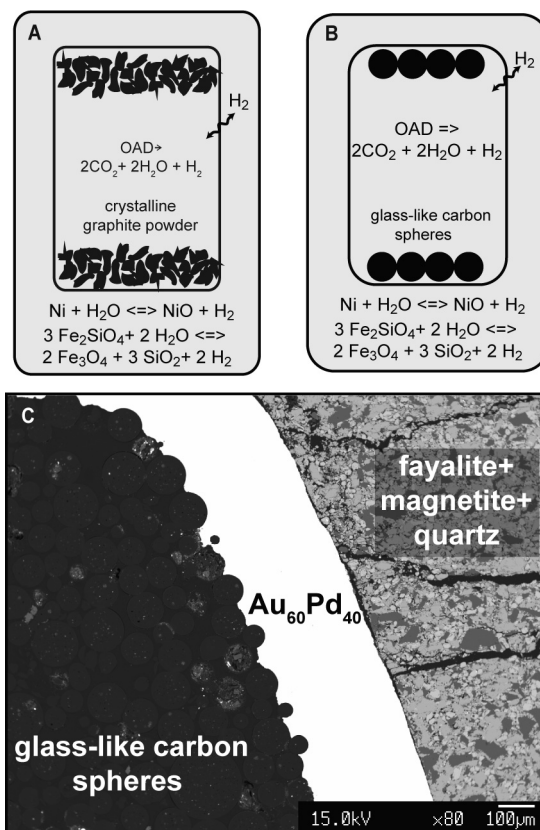
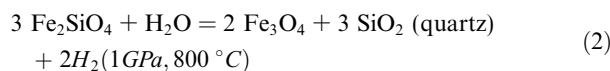
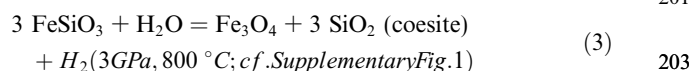


Fig. 1. Experimental setup. (A, B): sketch of the double capsule system. The inner Au–Pd capsule, permeable to H_2 , contains oxalic acid dihydrate (OAD), which decomposes at $T > 200$ °C to CO_2 , H_2O and H_2 , and either crystalline graphite (A) of glass-like carbon (B). The outer Au capsule contains the inner capsule and the fH_2 buffer, either fayalite-magnetite-quartz- H_2O or nickel-nickel-oxide- H_2O . The fH_2 constrained by the buffer is expected to be homogenous in the inner and in the outer capsule. (C): back-scattered electron image of the representative sample COH62 ($P = 1$ GPa and $T = 800$ °C) across the inner Au–Pd capsule boundary, showing glass-like carbon spheres on the left and the fayalite-magnetite-quartz buffer on the right.



In the inner capsule, the equilibration of the COH fluid is accomplished by the fH_2 -dependent coupled reactions (Tumiati et al., 2017):



As a consequence, the initial fluid composition (H_2O : $CO_2 = 1:1$ starting from OAD) adjusts its CO_2 fraction until equilibrium in fH_2 is reached between the inner and the outer capsule. The oxygen fugacity (fO_2) in the inner capsule (containing mixed H_2O – CO_2 fluids instead of pure water) is constrained indirectly and it will be slightly lower compared to the fO_2 constrained in the outer capsule (con-

221 taining pure H₂O) by FMQ and NNO (cf. Luth, 1989) and
222 it is calculated by thermodynamic modeling (see Section 2.5
223 and Table 2), ranging from ΔFMQ ($=\log f\text{O}_2^{\text{sample}} - \log \log$
224 $f\text{O}_2^{\text{FMQ}}$) -0.5 to -0.8 .

225 High-pressure pyrolysis of glucose to char has been con-
226 ducted in unbuffered single Au capsules (OD = 3 mm)
227 welded shut after filling with anhydrous glucose
228 (C₆H₁₂O₆, or CH₂O) produced by dehydration at 70 °C
229 (2 h) of α -D-glucose monohydrate (Sigma Aldrich)
230 (Ponschke and House, 2011).

231 2.2. Experimental conditions and apparatus

232 Experiments were performed at 1 and 3 GPa at 800 °C
233 using an end-loaded piston-cylinder apparatus. Capsules
234 were embedded in MgO rods (Norton Ceramics) and
235 inserted in graphite furnaces surrounded by NaCl and
236 borosilicate glass (Pyrex). At the top of the assembly, a
237 pyrophyllite–steel plug was placed to ensure the electrical
238 contact. Temperatures were measured with K-type thermo-
239 couples and are considered accurate to ± 5 °C. An alumina
240 disk was placed at the top of the capsule to avoid the direct
241 contact with the thermocouple. Pressure calibration of the
242 apparatus is based on the quartz to coesite transition
243 according to Bose and Ganguly (1995) (accuracy ± 0.01
244 GPa). Samples were first pressurized at run pressure, then
245 heated to $T = 800$ °C, with a ramp of 100 °C/min. Experi-
246 ments were quenched by turning off the power supply,
247 resulting in a rate of temperature decline of >40 °C/sec.
248 The double capsules were prepared by peeling off the outer
249 capsule, then heated at 110 °C in a vacuum oven (>2 h) to
250 remove any residual water trapped in the buffer. After the
251 analysis of volatiles (see below), double capsules were
252 mounted in epoxy resin and polished for scanning electron
253 microscopy and micro-Raman spectroscopy. The persis-
254 tence of the buffering assemblages was always verified by
255 means of electron microprobe analyses. Single capsules
256 containing char derived from the decomposition of anhy-
257 drous glucose were analyzed for volatiles, then opened to
258 collect the sample, which has been analyzed by scanning
259 electron microscopy, micro-Raman spectroscopy and syn-
260 chrotron X-ray diffraction.

261 2.3. Analysis of solids

262 Solid carbon in both buffered and unbuffered runs has
263 been characterized by scanning electron microscopy,
264 micro-Raman spectroscopy and synchrotron X-ray diffrac-
265 tion. Graphite and glass-like carbon were analyzed both as
266 starting materials and after quench from run P – T
267 conditions.

268 Quantitative analyses and back-scattered electron imag-
269 ing of the experimental products were performed to check
270 the integrity of the buffering mineral assemblages, using a
271 JEOL 8200 wavelength-dispersive (WDS) electron micro-
272 probe, at 15 kV accelerating potential, 5 nA sample current
273 and 1 μm beam size. Standards used were fayalite (Fe), nic-
274 colite (Ni) and grossular (Si). A counting time of 30 s (10 s
275 background) was used for all the elements. Secondary

electron imaging of pyrolytic carbon has been performed 276
at 15 kV and 0.05 nA sample current. 277

278 Micro-Raman spectra were acquired using the inte-
279 grated micro/macro-Raman LABRAM HRVIS (Horiba
280 Jobin Yvon Instruments) of the Interdepartmental Center
281 “G. Scansetti” (Department of Earth Sciences, University
282 of Torino, Italy). Excitation lines at 532 nm (solid-state
283 Nd laser and 80 mW of emission power) were used with
284 Edge filter and a grating of 600 grooves/mm. Calibration
285 was performed using the 520.6 cm⁻¹ Si band. The laser
286 power on the sample was set upon the measured materials
287 at 2 mW by the addition of filters. Acquisition times were
288 set at 25 s for 3 accumulations with a laser spot of 2 μm .

289 X-ray Powder diffraction (XRD) data were obtained at
290 XRD1 beamline (Elettra, Trieste, Italy). The samples were
291 placed in glass capillaries and mounted onto the head of the
292 Huber Kappa Goniometer installed at the beamline. The
293 data were collected with a monochromatic radiation
294 ($\lambda = 0.7000$ Å), using a Dectris Pilatus 2 M detector. The
295 beam size at the sample was of 0.2 \times 0.7 mm and the cali-
296 bration of the set-up geometry was checked with a LaB₆
297 pattern. Successively, the images were integrated with
298 Fit2D software package (Hammersley et al., 1995; Ham-
299 mersley, 1997) and analyzed using the GSAS EXPGUI
300 software (Toby, 2001).

301 2.4. Analysis of volatiles

302 For the analysis of quenched volatiles in the capsules
303 (Table 1) we employed the capsule-piercing technique
304 (Tiraboschi et al., 2016). Volatiles, heated to $T \approx 80$ °C to
305 allow liquid water to be converted into water vapor, were
306 extracted from the capsules in a Teflon reactor and con-
307 veyed to a quadrupole mass spectrometer (EXXTORR 0–
308 200 amu, Mod. XT 200, equipped with secondary electron
309 multiplier) using ultrapure Ar as carrier gas. The pressure
310 conditions in the reactor were monitored through high-
311 resolution sensor gauges (± 1 mbar precision). The temper-
312 ature in the reactor was monitored with K-type thermocou-
313 ple. Gas mixtures of known compositions and ultrapure
314 water were utilized for the calibration of the quadrupole
315 mass spectrometer. The technique enabled retrieval of
316 micromolar quantities of the volatiles H₂O, CO₂, CO,
317 CH₄, H₂ and O₂ with uncertainties of ~ 1 mol% (10 mol%
318 for CO, due to the interference with atmospheric N₂ on
319 the 28 m/z channel). The periodic analysis of test capsules
320 filled with 1 mg of oxalic acid dihydrate, thermally decom-
321 posed at 250 °C to H₂O, CO, CO₂ and H₂ (Tiraboschi et al.,
322 2016), ensures the stability and the reproducibility of the
323 analyses over time.

324 2.5. Thermodynamic modeling

325 The volatile composition of carbon-saturated COH flu-
326 ids, and in particular their $X\text{CO}_2$ [$=\text{CO}_2/(\text{H}_2\text{O} + \text{CO}_2)_{\text{molar}}$]
327 in relatively oxidized systems, is dependent on the redox
328 state of the system (cf. the review of Tumiati and
329 Malaspina, 2019), which can be controlled indirectly in
330 experiments by fixing the hydrogen fugacity in double cap-
331 sules (e.g., Eugster and Skippen, 1967).

Table 1
Run table of the experiments and volatiles measured using the capsule-piercing technique.

| Run | P (GPa) | T (°C) | capsule | buffer | runtime (h) | starting materials | total volatiles (mmol) | H ₂ O | CO ₂ | CO | CH ₄ | H ₂ | XCO ₂ |
|--------|---------|--------|---------|--------|-------------|--------------------------------------|------------------------|------------------|-----------------|----------|-----------------|----------------|------------------|
| COH69 | 1 | 800 | double | FMQ | 88 | OAD + graphite | 8.14 | 2.40(6) | 4.98(3) | 0.00(60) | 0.02(5) | 0.00(1) | 0.674(7) |
| COH70 | 1 | 800 | double | NNO | 92 | OAD + graphite | 7.21 | 1.80(6) | 4.87(3) | 0.00(59) | 0.02(5) | 0.02(1) | 0.731(8) |
| COH76 | 3 | 800 | double | FMQ | 48 | OAD + graphite | 5.51 | 1.19(2) | 3.43(1) | 0.03(24) | 0.00(2) | 0.000(5) | 0.74(2) |
| COH105 | 3 | 800 | double | FMQ | 24 | H ₂ O + graphite | 11.2 | 2.51(5) | 6.28(2) | 0.76(39) | 0.04(3) | 0.00(1) | 0.714(5) |
| COH103 | 3 | 800 | double | NNO | 24 | OAD + graphite | 49.5 | 47.1(2) | 4.86(8) | 0.5(1.5) | 0.02(13) | 0.00(3) | 0.094(1) |
| COH62 | 1 | 800 | double | FMQ | 24 | OAD + glass-like carbon | 7.34 | 1.21(6) | 4.84(3) | 0.00(64) | 0.01(6) | 0.00(1) | 0.801(9) |
| COH57 | 1 | 800 | double | NNO | 24 | OAD + glass-like carbon | 6.88 | 0.89(4) | 5.03(2) | 0.00(42) | 0.02(4) | 0.00(1) | 0.850(6) |
| COH112 | 3 | 800 | double | FMQ | 24 | OAD + glass-like carbon | 8.73 | 2.93(11) | 3.84(5) | 0.07(93) | 0.02(8) | 0.00(2) | 0.57(1) |
| COH108 | 3 | 800 | double | FMQ | 24 | H ₂ O + glass-like carbon | 8.31 | 2.59(21) | 2.59(9) | 0(2) | 0.09(14) | 0.00 | 0.50(3) |
| COH100 | 3 | 800 | double | NNO | 24 | OAD + glass-like carbon | 20.7 | 15.83(2) | 1.74(1) | 0.06(19) | 0.02(02) | 0.334(4) | 0.099(1) |
| COH122 | 1 | 800 | single | - | 12 | glucose anhydrous | 23.31 | 14.27(1) | 1.10(1) | 0.58(11) | 5.04(2) | 0.005(4) | 0.072(1) |
| COH124 | 1 | 800 | single | - | 24 | glucose anhydrous | 52.40 | 38.8(2) | 12.3(1) | 0(1) | 2.3(2) | 0.00(6) | 0.240(3) |
| COH123 | 3 | 800 | single | - | 24 | glucose anhydrous | 60.74 | 48.1(6) | 0.48(1) | 0.48(5) | 0.05(1) | 0.000(2) | 0.0098(3) |

Standard deviation (2 sigma) expressed in bracket notation.

FMQ: fayalite-magnetite-quartz-H₂O (ferrosilite-magnetite-coesite-H₂O at 3 GPa, 800 °C).

NNO: nickel-nickel oxide-H₂O.

OAD: oxalic acid dehydrate.

XCO₂ = CO₂/(H₂O + CO₂)molar.

The fugacities of oxygen and hydrogen in the outer and in the inner capsules at NNO and FMQ conditions were calculated using the Perple_X package (Connolly, 2005), using the thermodynamic dataset of Holland and Powell (Holland and Powell, 1998) revised by the authors in 2004 (hp04ver.dat), the Perple_X water equation of state (EoS) “H–O HSMRK/MRK hybrid”, and using the Excel spreadsheet GFluid (Zhang and Duan, 2010) with the COH fluid EoS of Zhang and Duan (2009), which is based on the equilibrium constants K_P of the following reactions:



Tumiati et al. (2017) showed that the composition of graphite-saturated COH fluids at 1–3 GPa and 800 °C are reproduced best using a modified version of Zhang and Duan’s model, implemented with f_{H_2} coefficients (γ_{H_2}) changing dynamically as a function of $X(O) [=O_2/(H_2 + O_2)_{molar}]$, taken from the EoS of Connolly and Cesare (1993). Therefore, in this study we refer to this modified model to (i) predict the composition of buffered fluids in equilibrium with crystalline graphite (Table 2); (ii) compare it with the measured composition of fluids in equilibrium with either crystalline graphite or glass-like carbon (Fig. 2; Table 1) and (iii) retrieve the difference in free energy between graphite and glass-like carbon (ΔG), by iteratively changing the Zhang and Duan’s K_P s (cf. Eqs. (4)–(7)) to account for the measured XCO_2 of fluids in equilibrium with the latter phase (Table 3). The experimental ΔG was compared with the ΔG predicted by thermodynamic modeling, performed with thermodynamic parameters retrieved from literature added to the database of Holland and Powell (hp04ver.dat) (Table 4), thus making feasible with Perple_X the calculation of $G-P$ and $\log f_{O_2}(P, T)$ phase diagrams involving glass-like carbon in addition to crystalline graphite.

Recent studies outlined the importance of non-volatile charged carbon species (not detectable with the capsule-piercing technique) and/or organic dissolved compounds in high-pressure COH fluids at certain $P-T-f_{O_2}$ -pH conditions (Sverjensky et al., 2014a,b; Pan and Galli, 2016; Tiraboschi et al., 2018; Huang and Sverjensky, 2019). In particular, Sverjensky et al. (2014a,b) showed that at high pH values aqueous bicarbonate and carbonate species become dominant instead of molecular CO₂ and CH₄. In addition, organic dissolved species (e.g., formates and acetates) may form at ultra-high pressures (e.g., 5 GPa at 600 °C in Sverjensky et al., 2014a,b). Therefore, conventional thermodynamic models (Connolly and Cesare, 1993; Zhang and Duan, 2009), which consider neutral molecular species only, are not always adequate to predict carbon speciation in subduction fluids. It is an open question whether the available thermodynamic models are still valid in the presence of COH fluid immiscibility, suggested at $P = 1.5–2.5$ GPa and $T = 600–700$ °C in graphite-saturated slightly saline fluids (Li, 2016) and in low-

Table 2

Thermodynamic modelling of graphite-saturated fluids buffered at the investigated P – T – fH_2 conditions.

| P (GPa), T (°C) | 1, 800 | 1, 800 | 3,800 | 3, 800 |
|--|--------|--------|--------|--------|
| buffer | NNO | FMQ | NNO | FMQ |
| $\log fO_2$ outer capsule ^a | –13.47 | –13.70 | –12.62 | –11.19 |
| $\log fH_2$ outer capsule = inner capsule ^b | 1.775 | 1.889 | 3.107 | 2.361 |
| Modeled composition at fixed fH_2 (mol%) | | | | |
| H ₂ O | 28.74 | 34.25 | 65.34 | 26.60 |
| CO ₂ | 70.46 | 64.93 | 34.59 | 73.33 |
| CO | 0.66 | 0.64 | 0.05 | 0.07 |
| CH ₄ | 0.06 | 0.09 | 0.02 | 0.00 |
| H ₂ | 0.08 | 0.09 | 0.01 | 0.00 |
| χCO_2 ^d | 0.710 | 0.655 | 0.346 | 0.733 |
| χO ^e inner capsule | 0.746 | 0.705 | 0.507 | 0.765 |
| $\log fO_2$ inner capsule | –14.28 | –14.31 | –11.99 | –11.66 |
| ΔFMQ ^f inner capsule | –0.58 | –0.61 | –0.80 | –0.47 |
| pH ^g | 3.25 | 3.26 | 2.34 | 2.22 |

^aEoS by Zhang and Duan (2009) with dynamic γH_2 taken from Connolly and Cesare (1993), changing as a function of P , T and χO ($\gamma H_2 = A \times (\chi O)^3 + B \times (\chi O)^2 + C \times \chi O + D$; where $A = 43.919$, $B = 114.55$, $C = -105.75$, $D = 41.215$ at 1 GPa–800 °C; $A = -11208$; $B = 26723$, $C = -21949$, $D = 6979.2$ at 3 GPa–800 °C).

^a retrieved using the Perple_X package and the hp02ver.dat database (see also Supplementary Fig. 4), considering the reactions: i) $2 Ni + O_2 = 2 NiO$; ii) $3 Fe_2SiO_4 + O_2 = 2 Fe_3O_4 + 3 SiO_2$ (1 GPa–800 °C; quartz stable) and iii) $3FeSiO_3 + O_2 = Fe_3O_4 + 3 SiO_2$ (3 GPa–800 °C; coesite stable).

^b retrieved using the routine “fluids” of the Perple_X package (H-O HSMRK/MRK hybrid EoS).

^d $\chi CO_2 = CO_2 / (H_2O + CO_2)_{molar}$

^e $\chi O = O_2 / (H_2 + O_2)_{molar}$

^f $\Delta FMQ = \log fO_2 - \log fO_2^{FMQ}$

^g retrieved using the Deep Earth Water model by fixing the fO_2 of the inner capsule; neutral pH at 1 GPa–800 °C = 4.02; neutral pH at 3 GPa–800 °C = 3.09.

397 temperature/high-pressure hydrocarbon fluids (Huang
398 et al., 2017). In particular, Li (2016) found at 2.5 GPa
399 and 700 °C at Re–ReO₂ redox conditions ($\approx \Delta FMQ = +2$)
400 mixed H₂O–CO₂ fluids in equilibrium with almost pure
401 CO₂. As the capsule-piercing technique used in our study
402 only allows measurement of the bulk volatile components,
403 it cannot be used to investigate fluid immiscibility. How-
404 ever, on the basis of the results given in our study and in
405 previous works (Matveev et al., 1997; Tiraboschi et al.,
406 2016; Tumiati et al., 2017), the conventional models are still
407 able to predict the bulk composition (but not necessarily the
408 speciation) of high-pressure fluids in terms of bulk CO₂/
409 (H₂O + CO₂) and CH₄/(H₂O + CH₄), although they could
410 fail at certain P – T – fO_2 –pH conditions where species other
411 than H₂O, CO_{2(aq)} and CH_{4(aq)} become dominant. In order
412 to justify our experimental approach we used the Deep
413 Earth Water thermodynamic model (Sverjensky et al.,
414 2014a,b) to confirm that molecular CO_{2(aq)} is by far the
415 dominant carbon-bearing fluid species at our experimental
416 conditions, and to estimate the pH of the fluids (Table 2).

3. RESULTS

3.1. Characterization of solid carbon

3.1.1. Crystalline graphite

420 Back-scattered electron observation of graphite powder
421 used as starting material did not reveal any foreign mater-
422 rial. The powder consists of homogeneous flakes with grain
423 size of 10–100 μm (Supplementary Fig. 2a). X-ray powder

424 diffraction showed that the powder is monomineralic and
425 crystalline, with a sharp diffraction peak at
426 $d_{002} = 3.3672 \text{ \AA}$ (Supplementary Fig. 3 – graphite). Fitted
427 pattern showed that the averaged crystallite size of the sam-
428 ple is around 50 nm. Micro-Raman spectroscopy of unpol-
429 ished graphite powder showed a sharp graphite (G) peak at
430 1600 cm^{-1} and only a little disorder (D) peak at 1350 cm^{-1} ,
431 confirming that this material is highly ordered (Ferrari,
432 2007) (Supplementary Fig. 4). The G' peak (also called
433 $2D$ in Ferrari, 2007) at about 2700 cm^{-1} is also well devel-
434 oped. Raman spectra of polished graphite showed a
435 marked increase of the D peak owing to mechanical modi-
436 fications during the polishing (Pasteris, 1989), and was
437 therefore not considered. Quenched graphite samples did
438 not show any evidence of substantial modification with
439 respect to starting graphite powder, within the uncertainties
440 caused by polishing.

3.1.2. Glass-like carbon

441 Glass-like carbon spheres used as starting material
442 appeared homogenous at the scanning electron microscope.
443 They are about 100 μm in size, and show sparse closed
444 porosity (Supplementary Fig. 2b). X-ray powder diffraction
445 of the spherical powder showed broad peaks, typical of
446 amorphous materials (Supplementary Fig. 3). Micro-
447 Raman spectra show broad G and D peaks, which charac-
448 terize amorphous sp^2 carbon (cf. Ferrari and Robertson,
449 2001), with D peak $>$ G peak (Fig. 2). The G' peak is poorly
450 developed. Glass-like carbon retrieved after runs showed
451 Raman spectra identical to the starting material.
452

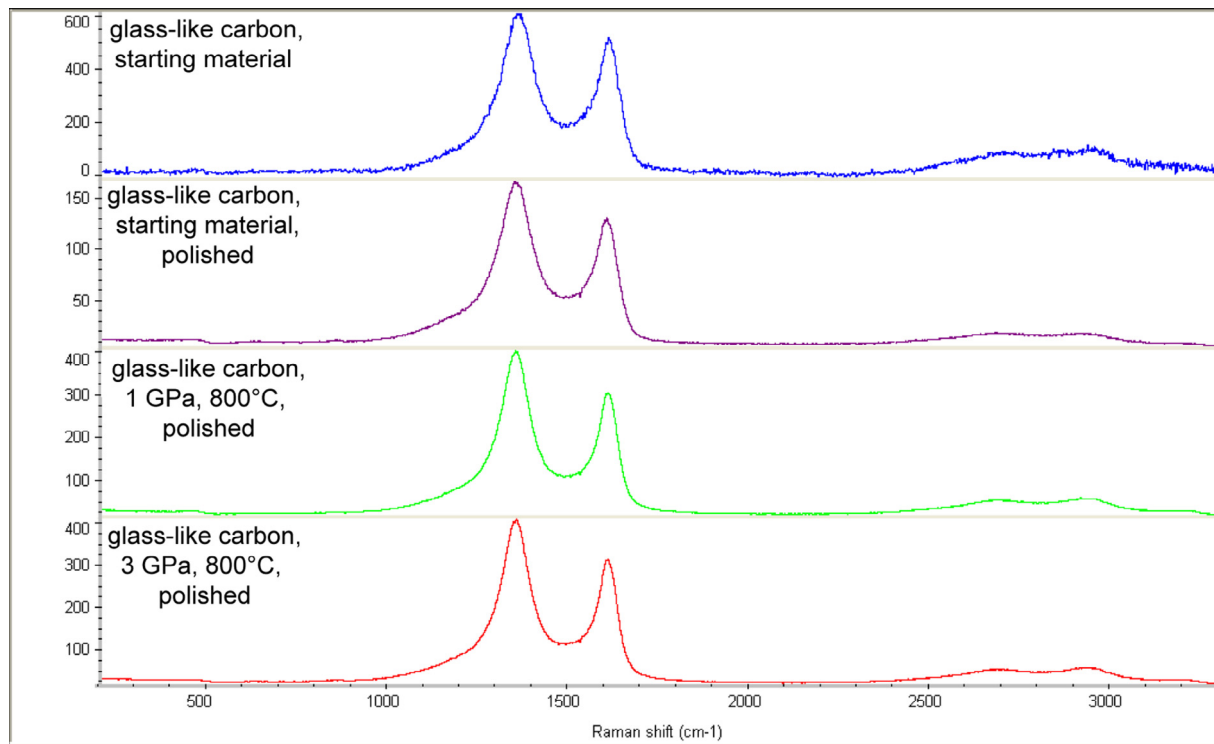


Fig. 2. Micro-Raman spectra of glass-like carbon as starting material (unpolished: blue; polished: purple) and as quenched product from 1 GPa–800 °C (green) and from 3 GPa–800 °C (red). (For interpretation of the references to colour in this figure legend, the reader is referred to the web version of this article.)

Table 3

Equilibrium constants (K_P) at $T = 800$ °C and difference in Gibbs free energy of glass-like carbon with respect to crystalline graphite (ΔG), retrieved from measured fluid composition.

| Carbon form | graphite | glass-like carbon | glass-like carbon | graphite | glass-like carbon | glass-like carbon |
|--|--------------------|--------------------|--------------------|--------------------|--------------------|--------------------|
| Pressure GPa | 1 | 1 | 1 | 3 | 3 | 3 |
| Buffer | - | NNO | FMQ | - | NNO | FMQ |
| $\log K_P \text{ C} + \text{O}_2 = \text{CO}_2$ | 44.98 ^a | 45.16 ^b | 45.17 ^b | 46.12 ^a | 46.18 ^b | 45.86 ^b |
| $\log K_P \text{ C} + 0.5 \text{ O}_2 = \text{CO}$ | 23.77 ^a | 23.95 ^b | 23.96 ^b | 24.91 ^a | 24.97 ^b | 24.65 ^b |
| $\log K_P \text{ C} + 2 \text{ H}_2 = \text{CH}_4$ | -2.48 ^a | -2.30 ^b | -2.29 ^b | -1.33 ^a | -12.7 ^b | -1.59 ^b |
| ΔG (kJ mol ⁻¹) ^c | - | 1.6(1) | 1.7(1) | - | 0.51(1) | -2.3(2) |

^a EoS by Zhang and Duan (2009) (GFluid), at $T = 800$ °C.

^b calculated by simulation analysis to fit measured X_{CO_2} ($=\text{CO}_2/\text{H}_2\text{O} + \text{CO}_2$) of samples COH57, COH62, COH100 and COH112, assuming constant f_{H_2} .

^c $\Delta G = G_{\text{glass-like C}} - G_{\text{graphite}}$ at $T = 800$ °C, calculated using the equation: $\Delta G = RT \times \ln (K_P^{\text{glass-like C}}/K_P^{\text{graphite}})$; the uncertainty in ΔG (bracket notation) has been calculated taking into account the standard deviation of QMS analyses (Table 1).

3.1.3. Char from high-pressure pyrolysis of anhydrous glucose

Secondary electron imaging of solid carbon formed by decomposition of glucose (char) at 1–3 GPa and 800 °C show microtextures that are dependent on the run duration. In the 12-h run at 1 GPa, char comes as a loose spherical powder with an average grain size of 1 μm (Fig. 3a, b). In the 24-h runs at 1 and 3 GPa, spherical elements are not visible, and char is characterized by a glass-like appearance with conchoidal fracture and absence of cleavage (Fig. 3c–f). X-ray powder diffractions of char (Supplementary Fig. 3) show that the diffraction angle of the most intense peak is lower compared to that of crystalline gra-

phite, while the full width at half maximum (FWHM) is higher, meaning a decline of the crystallite size. The crystallite size of char synthesized at the investigated high-pressure conditions is of about 2–4 nm typical of nano-crystalline materials. The Raman spectra of char synthesized at 1 and 3 GPa in 24-h long runs are very similar, with broad G and D peaks ($D > G$) (Fig. 4). Compared to glass-like carbon, the D peak is slightly higher, but broadening of the peaks is a little less pronounced. The G' peak is comparable to that of glass-like carbon. The Raman spectrum of char synthesized at 1 GPa in the shorter 12-h run is characterized by similar G and D peaks, but remarkably higher G' peak

Table 4

Thermodynamic properties of graphite and glass-like carbon (preferred model) at different pressures and temperatures.

| <i>P</i> GPa | 1.00E-04 | 1 | 3 | 1.00E-04 | 1 | 3 |
|--|----------------------|-------|--------|----------|--------|-------|
| <i>T</i> °C | 25 standard state | 25 | 25 | 800 | 800 | 800 |
| <i>graphite</i> | | | | | | |
| $G_{P,T}$ kJ/mol | 0.000 | 5.195 | 15.309 | -12.866 | -7.529 | 2.763 |
| $S_{P,T}$ J/mol/K | 5.74 | 5.64 | 5.49 | 26.04 | 25.88 | 25.61 |
| $V_{P,T}$ J/mol/bar | 0.53 | 0.52 | 0.50 | 0.54 | 0.53 | 0.50 |
| $K_{P,T}$ GPa | 33.8 | 42.8 | 60.6 | 30.1 | 39.1 | 57.0 |
| K' | 8.9 | 8.9 | 8.9 | 8.9 | 8.9 | 8.9 |
| <i>glass-like carbon (preferred model)</i> | | | | | | |
| $G_{P,T}$ kJ/mol | 2.357 | 7.398 | 16.350 | -11.142 | -6.018 | 2.982 |
| $S_{P,T}$ J/mol/K | 6.60 | 6.53 | 6.53 | 26.90 | 26.77 | 26.69 |
| $V_{P,T}$ J/mol/bar | 0.53 | 0.48 | 0.42 | 0.54 | 0.49 | 0.42 |
| $K_{P,T}$ GPa | 9.0 | 11.9 | 17.6 | 8.0 | 10.8 | 16.5 |
| K' | 2.9 | 2.9 | 2.9 | 2.9 | 2.9 | 2.9 |
| ΔG kJ/mol | 2.357 | 2.203 | 1.041 | 1.724 | 1.511 | 0.219 |

Graphite parameters after Day (2012).

 $\Delta G = G_{P,T}$ (glass-like carbon) – $G_{P,T}$ (graphite). G_f^0 and S^0 of glass-like carbon: fit Gutzow (2005) (G – T data at ambient pressure). V^0 of glass-like carbon assumed identical to graphite. K^0 and K' of glass-like carbon: fit Zhao et al. (2014) (data at 25 °C from 1 to 3 GPa; glass-like carbon type I).

478 (Supplementary Fig. 5), which characterizes crystalline gra-
479 phite (Fig. 4).

480 3.2. Characterization of the fluid phase

481 Volatiles in all the experimental runs have been mea-
482 sured by means of the capsule-piercing technique (see
483 details in Tiraboschi et al., 2016) (Table 1; Fig. 5; Supple-
484 mentary Fig. 6). Total measured volatiles range from 5.51
485 to 49.5 micromoles in double capsules where fluids were
486 interacting with either crystalline graphite or glass-like car-
487 bon, and from 23.21 to 60.74 micromoles in single capsules
488 where fluids were produced by complete dehydration of
489 anhydrous glucose due to the reaction:



493 3.2.1. Buffered COH fluids interacting with crystalline 494 graphite

495 Fluids synthesized at 1–3 GPa and 800 °C contain
496 mostly H₂O and CO₂, with only traces of CO, CH₄ and
497 H₂ (typically close to or below the detection limit). At
498 $P = 1$ GPa, X_{CO_2} ($=\text{CO}_2/\text{H}_2\text{O} + \text{CO}_2^{\text{molar}}$) ranges from
499 0.674 ± 0.007 ($f\text{H}_2^{\text{FMQ}}$) to 0.731 ± 0.008 ($f\text{H}_2^{\text{NNO}}$). Because
500 the FMQ and NNO buffers cross at about 1.5 GPa (cf. Sup-
501 plementary Fig. 1), meaning that the NNO buffer is more
502 oxidizing than FMQ at $P < 1.5$ GPa and less oxidizing at
503 $P > 1.5$ GPa, fluids at $P = 3$ GPa buffered by NNO are
504 expected to show lower X_{CO_2} compared to fluids buffered
505 by FMQ (Table 2). At $f\text{H}_2^{\text{FMQ}}$, the run COH76, containing
506 oxalic acid dihydrate (OAD) as starting source of fluid, dis-
507 plays $X_{\text{CO}_2} = 0.74 \pm 0.02$, and run COH105, containing
508 water instead of OAD, displays a similar X_{CO_2} of 0.714
509 ± 0.05 . Instead, at $f\text{H}_2^{\text{NNO}}$ conditions the fluid phase is

dominated by water, resulting an X_{CO_2} of 0.094 ± 0.001
in run COH103.

519 3.2.2. Buffered COH fluids interacting with glass-like carbon

520 Fluids interacting with glass-like carbon at 1–3 GPa and
521 800 °C, buffered by either FMQ or NNO, contain only
522 traces of CO, CH₄ and H₂, as in the case of graphite-
523 saturated fluids (Table 1). However, the fluids with glasslike
524 carbon display different X_{CO_2} ratios to the graphite-
525 saturated ones (Fig. 5). In particular, fluids at 1 GPa are
526 display a higher CO₂ content, and are characterized by
527 X_{CO_2} of 0.801 ± 0.009 at $f\text{H}_2^{\text{FMQ}}$ and 0.850 ± 0.006 at $f\text{H}_2^{\text{NNO}}$,
528 corresponding to a higher content of +19 and
529 +16 mol% CO₂, respectively, if compared to graphite-
530 saturated fluids displaying $X_{\text{CO}_2} = 0.674$ at $f\text{H}_2^{\text{FMQ}}$ and
531 0.731 ± 0.008 at $f\text{H}_2^{\text{NNO}}$ (see above). However, the higher CO₂
532 compared with graphite-saturated fluids declines dramati-
533 cally at 3 GPa. At this pressure, fluids saturated with
534 glass-like carbon buffered at $f\text{H}_2^{\text{NNO}}$ show indeed a X_{CO_2}
535 of 0.099 ± 0.001 , corresponding to only +5 mol% CO₂
536 higher content relative to fluids saturated with graphite dis-
537 playing $X_{\text{CO}_2} = 0.094$. Fluids buffered at $f\text{H}_2^{\text{FMQ}}$ condi-
538 tions show CO₂ content that is even lower than that
539 characterizing graphite-saturated fluids. In fact, run
540 COH112 is characterized by $X_{\text{CO}_2} = 0.57 \pm 0.01$ (0.50
541 ± 0.03 in run COH108, with H₂O instead of OAD as start-
542 ing source of fluid), corresponding to a lower CO₂ content
543 of -24 mol% CO₂ relative to fluids saturated with graphite
544 ($X_{\text{CO}_2} = 0.74$; see above).

545 3.2.3. Unbuffered COH fluids generated by high-pressure 546 thermal decomposition of glucose

547 Fluids produced by high-pressure dehydration of anhy-
548 drous glucose display variable compositions, changing as a
549

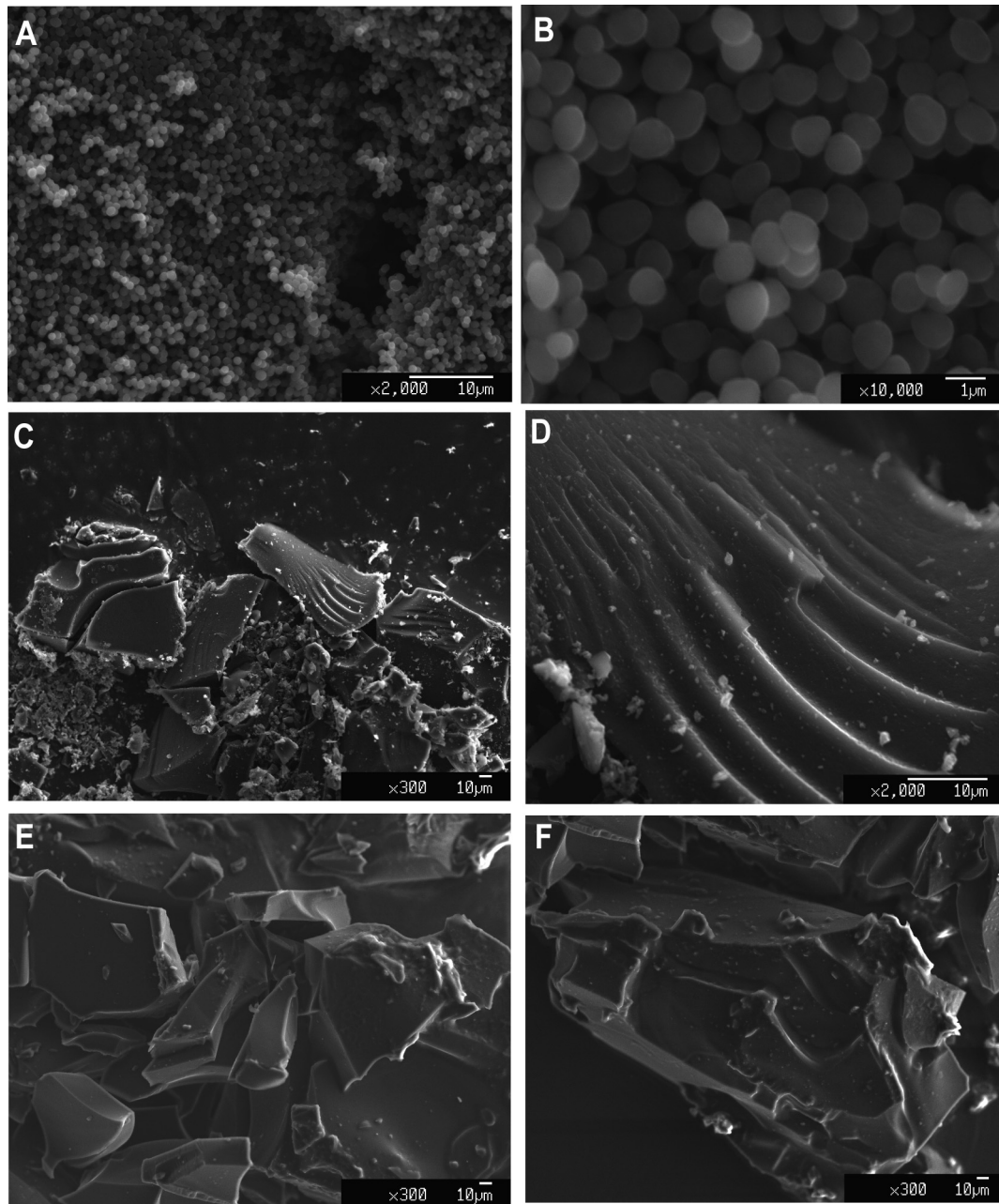


Fig. 3. Secondary electron images of char synthesized from glucose at 800 °C and high-pressure conditions. (A, B): $P = 1$ GPa, runtime 12 h; (C, D): $P = 1$ GPa, runtime 24 h; (E, F): $P = 3$ GPa, runtime 24 h.

542 function of run time and pressure conditions (Table 1; Sup-
 543 plementary Fig. 6). Fluids at 1 GPa show high contents of
 544 CH_4 , especially in run COH122 characterized by a rela-
 545 tively short runtime of 12 h. In this run, X_{CO_2} is 0.072
 546 ± 0.001 and $X_{\text{CH}_4} [= \text{CH}_4 / (\text{H}_2\text{O} + \text{CH}_4)_{\text{molar}}] = 0.261$.
 547 Fluid in run COH124, characterized by a longer duration
 548 of 24 h, displays a higher X_{CO_2} of 0.240 ± 0.003 and a
 549 lower CH_4 content ($X_{\text{CH}_4} = 0.056$). Fluid at 3 GPa (24 h)
 550 is nearly pure water with $X_{\text{CO}_2} = 0.0098 \pm 0.0003$ and
 551 $X_{\text{CH}_4} = 0.001$.

4. DISCUSSION

4.1. Comparison between experimental results and available thermodynamic models of fluids in equilibrium with crystalline graphite

The measured compositions of COH fluids interacting with crystalline graphite at 1 GPa and 800 °C (Table 1) is in excellent agreement, in both FMQ- and NNO-buffered experiments, with the compositions predicted at equilib-

552

553

554

555

556

557

558

559

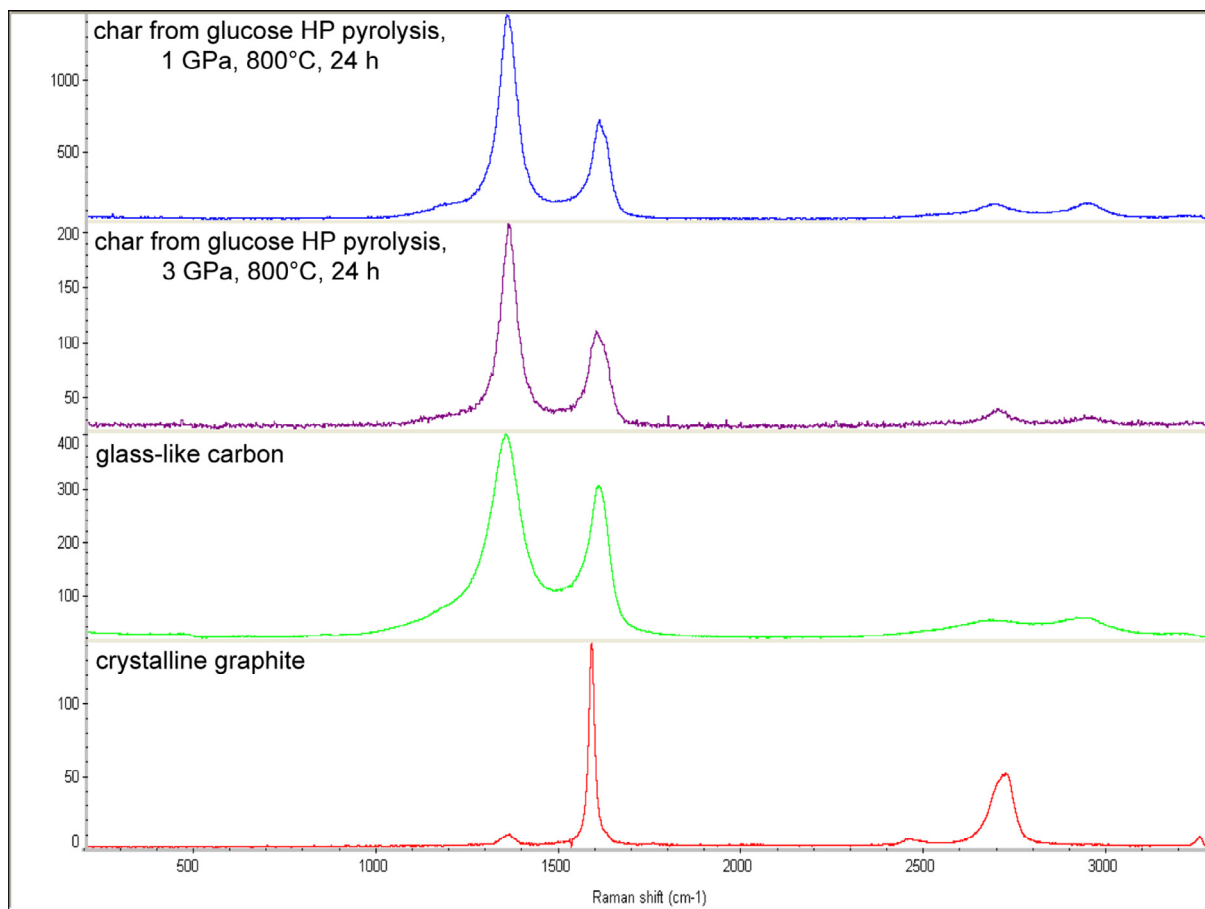


Fig. 4. Raman spectra of quenched char (1 GPa: blue; 3 GPa: purple) compared with glass-like carbon (green) and crystalline graphite (red). (For interpretation of the references to colour in this figure legend, the reader is referred to the web version of this article.)

560 rium conditions by the modified thermodynamic model of
 561 Zhang and Duan (2009) (Table 2; see details of the model
 562 in Section 2.5). At 3 GPa, while the fH_2^{FMQ} -buffered fluid
 563 matches the composition predicted by the model, the measured
 564 composition of the fluid buffered externally by NNO
 565 is characterized by a lower content of CO_2 . The measured
 566 XCO_2 would be consistent with an inner-capsule $\log fO_2$
 567 of -12.56 , instead of the predicted value of -11.99 (Table 2).
 568 At this stage, we can only speculate that this could be
 569 ascribed to uncertainties associated to the nickel–nickel
 570 oxide buffer (c.f. O'Neill and Pownceby, 1993), which could
 571 affect the estimates of fO_2 and fH_2 imposed by the NNO
 572 buffer at 3 GPa.

573 Some recent studies underlined the importance of the
 574 variable pH in governing the abundance of dissolved
 575 organic species and charges species (e.g., bicarbonates, car-
 576 bonates) instead of molecular species (Sverjensky et al.,
 577 2014a,b; Pan and Galli, 2016). Therefore, we used the Deep
 578 Earth Water (DEW) model (Sverjensky et al., 2014a,b) to
 579 draw pH vs fO_2 diagrams showing the loci of points where
 580 graphite is stable in COH fluids at saturation conditions at
 581 1 GPa–800 °C (Fig. 6a) and 3 GPa–800 °C (Fig. 6b) (black
 582 solid lines). The oxygen fugacities expected in COH fluids
 583 buffered at fH_2^{FMQ} and fH_2^{NNO} conditions are shown for refer-
 584 ence. The intersection of these oxygen fugacities with the

585 graphite-saturation curve represents the investigated exper-
 586 imental conditions (black dots), and thus provides an esti-
 587 mation of the pH value expected in the synthesized fluids,
 588 i.e. 3.5–3.6 at 1 GPa–800 °C (neutral pH = 4.02) and 2.22
 589 at 3 GPa–800 °C (neutral pH = 3.09). The model predicts
 590 that at the investigated P – T – fO_2 – fH_2 conditions the equi-
 591 librium between graphite and COH fluids is thus reached
 592 in the $CO_{2(aq)}$ stability field and at acidic conditions, which
 593 prevent the stability of carbonate and bicarbonate ions.
 594 $CO_{2(aq)}$ is therefore expected to be by far the dominant dis-
 595 solved carbon-bearing species, while other C–O–H species
 596 should occur in very minor amount, the most abundant
 597 being ethane ($\approx 10^{-4}$ mol%) at 1 GPa–800 °C and formic
 598 acid ($\approx 10^{-3}$ mol%) at 3 GPa–800 °C. Other organic and/
 599 or charged species display even lower abundances. This val-
 600 idates the methodological approach of this study, aiming to
 601 retrieve the composition of quenched fluids in terms of
 602 volatile molecular species, assuming that they represent
 603 the speciation at run conditions. As a corollary, the dia-
 604 grams in Fig. 6 suggest that when redox conditions are
 605 imposed on a petrological system (redox-buffered systems),
 606 the pH becomes merely a dependent variable, as long as
 607 graphite-saturation conditions persist. Conversely, in pH-
 608 buffered systems, the redox state would be controlled by
 609 pH.

585
586
587
588
589
590
591
592
593
594
595
596
597
598
599
600
601
602
603
604
605
606
607
608
609

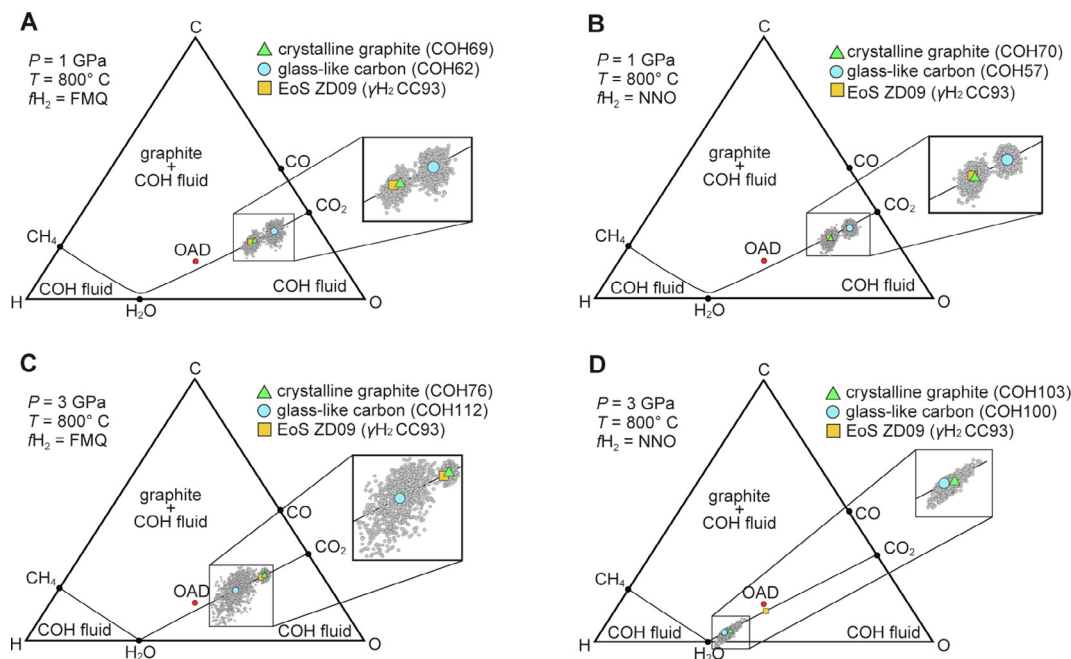


Fig. 5. Fluid compositions at the investigated P - T - fH_2 measured by using the capsule-piercing technique (Tiraboschi et al., 2016), plotted on ternary C-O-H diagrams. Green triangles: fluids in equilibrium with crystalline graphite. Blue dots: fluids in equilibrium with glass-like carbon. Yellow squares: composition of graphite-saturated fluids according to the modified model of Zhang and Duan (2009) (see text for details). Grey dots: analytical uncertainty cloud estimated by Monte Carlo method using the standard deviations provided in Table 1. (For interpretation of the references to colour in this figure legend, the reader is referred to the web version of this article.)

4.2. Experimental fluids in equilibrium with glass-like carbon and retrieval of its thermodynamic properties at high-pressure conditions

The CO_2 content of fluids interacting with glass-like carbon is different with respect to the CO_2 content of fluids in equilibrium with crystalline graphite (Fig. 5; Table 1). Fluids at 1 GPa are considerably enriched in CO_2 , while fluids at 3 GPa are only slightly enriched or even depleted with respect to graphite-saturated fluids. The observed difference is +19 mol% CO_2 at 1 GPa- fH_2^{FMQ} , +16 mol% CO_2 at 1 GPa- fH_2^{NNO} , +5 mol% at 3 GPa- fH_2^{FMQ} and -24 mol% CO_2 at 3 GPa- fH_2^{NNO} . These different fluid compositions are uniquely ascribable to difference between the thermodynamic properties of glass-like carbon and crystalline graphite. Taking as example Eq. (6) ($C + O_2 = CO_2$), the equilibrium constant of the reaction is:

$$K_p(T) = \frac{[CO_2]}{[O_2]} \quad (11)$$

where brackets indicate equilibrium concentrations of fluid phases over solid carbon.

At 1 GPa and 800 °C, involving perfectly crystalline graphite, the equilibrium constant of the reaction following the thermodynamic model of Zhang and Duan (2009) is 3.416×10^{19} ($\ln K_p = 44.98$). By changing K_p , the fluid CO_2 content predicted by the model changes accordingly. By means of iterative calculation, it is possible to find a K_p that fits the measured CO_2 value in runs where fluids reacted with glass-like carbon instead of graphite at the same P - T conditions. The equilibrium constant of a hetero-

geneous reaction with the participation of glass-like carbon (gl) instead of graphite (graph) can be expressed as:

$$K_{pgl}(T) = K_{pgraph}(T) \exp\left(\frac{\Delta G(T)}{RT}\right) \quad (12)$$

where $\Delta G(T)$ is the difference in Gibbs free energy between glass-like carbon $G_{gl}(T)$ and graphite- $G_{graph}(T)$, and R is the gas constant. This difference can be made explicit, resulting in the equation:

$$\Delta G(T) = RT \ln\left(\frac{K_{pgl}(T)}{K_{pgraph}(T)}\right) \quad (13)$$

As this difference in Gibbs free energy at fixed P - T - fH_2 must be the same for all the reactions (6), (7) and (9), by means of simulation analysis performed with the Solver tool in the Excel spreadsheet provided by Zhang and Duan (2010) we changed iteratively all the pertaining equilibrium constants simultaneously, imposing the mathematical constraint that the resulting ΔG is identical for all the equations, until the model converges to the measured X_{CO_2} . The retrieved ΔG and the equilibrium constants retrieved by simulation analysis at 1 and 3 GPa are shown in Table 3. ΔG is almost coincident in runs performed at NNO and FMQ conditions at 1 GPa-800 °C, where fluids equilibrated with glass-like carbon contain higher CO_2 fractions compared to graphite-saturated fluids. At these P - T conditions, ΔG is equal to +1.6(1) at fH_2^{NNO} and +1.7(1) kJ/mol at fH_2^{FMQ} . The difference in Gibbs free energy between graphite and glass-like at 1 GPa agree with previous studies performed at room pressure, where ΔG is +1.8 kJ/mol at 800 °C (Guencheva et al., 2001; Gutzow

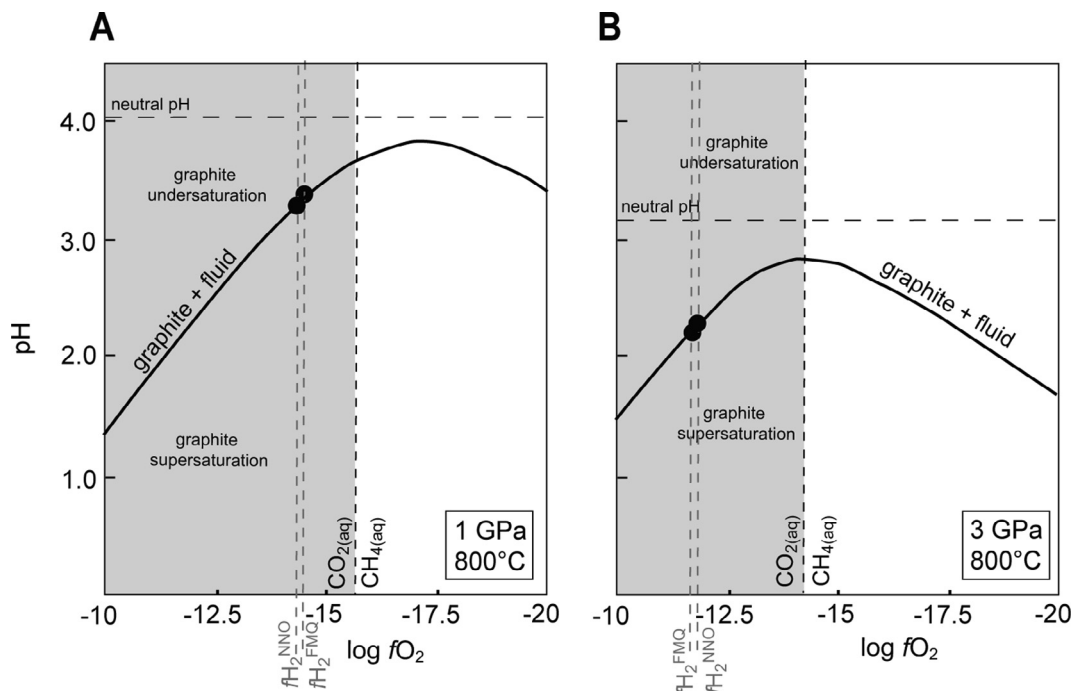


Fig. 6. $\log fO_2$ vs pH diagrams at 1 GPa–800 °C (A) and 3 GPa–800 °C (B), calculated using the Deep Earth Water model, showing the COH-graphite saturation curve (thick black). Black dots: experimental conditions at fH_2^{FMQ} and fH_2^{NNO} .

671 et al., 2005). At 3 GPa and 800 °C, fluids in equilibrium
 672 with glass-like carbon buffered at fH_2^{NNO} conditions display
 673 a slightly higher CO_2 content compared to graphite-
 674 saturated fluids, and ΔG is equal to +0.5(1) kJ/mol. Fluids
 675 buffered at fH_2^{FMQ} conditions show a CO_2 content which is
 676 even lower than fluids in equilibrium with graphite, corre-
 677 sponding to a negative ΔG of –2.3(2) kJ/mol.

678 4.3. Thermodynamic modeling of glass-like carbon and 679 implications for its stability towards graphite and diamond

680 We are not aware of previous Gibbs free energy of glass-
 681 like carbon at high pressures, even though layers of glass-
 682 like carbon spheres have long been employed in experimen-
 683 tal petrology as melt traps at pressure conditions ranging
 684 from 1 to 5 GPa (Robinson et al., 1998; Wasylenki, 2003;
 685 Dasgupta et al., 2005; Falloon et al., 2008; Spandler
 686 et al., 2008). Therefore, we derived the $G(P, T)$ curve of
 687 glass-like carbon at pressures up to 3 GPa (Fig. 7), by using
 688 the following thermodynamic parameters (Table 4; Supple-
 689 mentary Table 1):

- 690 • the standard Gibbs free energy of formation, retrieved
 691 from the G – T data of Guencheva et al. (2001) and
 692 Gutzow et al. (2005) at room pressure and $T = 298$ K
 693 ($\Delta_f G^0 = 2.357$ kJ/mol);
- 694 • the standard entropy (S_{298}^0), retrieved by fitting the G – T
 695 data at room pressure of Gutzow et al. (2005). The
 696 retrieved $S_{298}^0 = 6.6$ J/mol/K agrees well with the stan-
 697 dard entropy of 6.2 J/mol/K resulting from the integra-
 698 tion of low-temperature heat capacity $[C_P(T)]$
 699 measurements (Cappelletti et al., 2018), following:

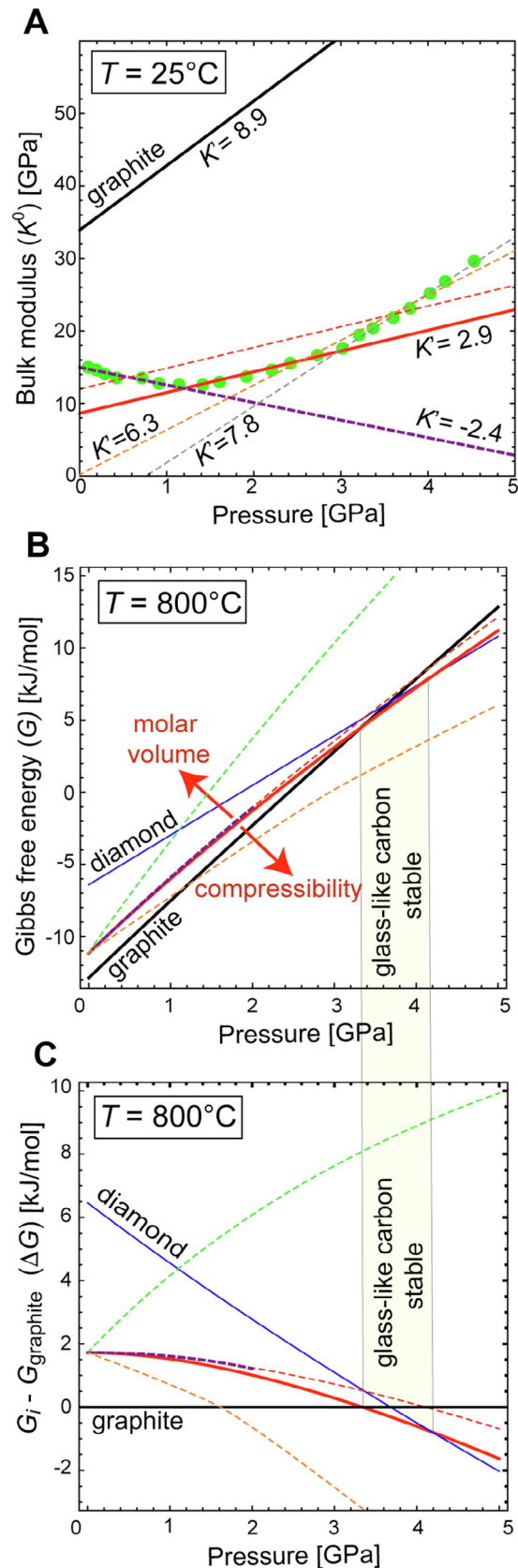
$$S_{298}^0 = S_0^0 + \int_0^{298} \left[\frac{C_P^0(T)}{T} \right] dT, \quad (14)$$

taking into account that S_0^0 , i.e. the residual entropy at 0 K,
 is non-zero in amorphous solids;

- 700 • the following parameters were assumed to be the same
 701 as for graphite (Holland and Powell, 1998; Day, 2012),
 702 as they have been reported to be very similar in glasslike
 703 carbon: i) the thermal expansion (cf. Coward and
 704 Lewis, 1967), ii) the coefficients of the heat capacity
 705 function (cf. Takahashi and Westrum, 1970;
 706 Yokoyama et al., 1971) and iii) the standard molar vol-
 707 ume, relying on the fact that the disordered multilayer
 708 graphene component in glass-like carbon has a density
 709 close to that of graphite (2.25 g/cm³) and the interplanar
 710 d -spacings are in broad agreement with those of graphite
 711 (Supplementary Fig. 3; cf. also Zhao et al., 2015; Hu
 712 et al., 2017). Models with molar volume increased by
 713 50%, reflecting the apparently lower bulk density of
 714 glass-like carbon (≈ 1.5 g/cm³; Coward and Lewis,
 715 1967; Zhao et al., 2015) imputable to the high closed
 716 porosity, are also provided for comparison in Fig. 7b–c.
 717 • the isothermal bulk modulus under standard conditions
 718 (K^0) and its first pressure derivative (K') were retrieved
 719 by linear regression of the data of type-I glass-like car-
 720 bon reported by Zhao et al. (2015) (green dots in
 721 Fig. 7a), where K^0 is the intercept at 0.0001 GPa
 722 (1 bar) at 25 °C and K' is the slope of the K – P curves.
 723 However, the estimation of glass-like carbon K^0 and
 724
 725
 726
 727
 728
 729

730 K' is not straightforward. Glass-like carbon displays a
 731 very high compressibility compared to graphite (cf. bulk
 732 modulus data in Day, 2012; Table 4), with a more than
 733 halved K^0 decreasing abnormally with increasing pres-
 734 sure up to 1 GPa (i.e., negative $K' = -2.4$, correspond-
 735 ing to a K^0 intercept of 15 GPa; purple thick dashed lines in
 736 Fig. 7), followed by a reversal to positive pressure
 737 dependence, accounting to a K' of 2.9 in the 1–3 GPa
 738 pressure range (extrapolated $K^0 = 9$ GPa; red thick lines
 739 in Fig. 7; preferred model as it is consistent with the
 740 pressures investigated in this study and with K^0 of other
 741 forms of non-graphitic sp^2 -type carbon; cf. fullerene in
 742 Sundqvist and Olabi, 2016) and $K' = 7.8$ at pressures
 743 above 3 GPa (extrapolated $K^0 = -6$ GPa; grey dashed
 744 lines in Fig. 7). In Fig. 7b, we show how the choice of
 745 different K^0 and K' values affects the $G(P, 800^\circ\text{C})$ of
 746 glass-like carbon with pressure increasing from 0 to 5
 747 GPa. The predicted difference in Gibbs free energy at
 748 800°C versus pressure between glass-like carbon and
 749 graphite (ΔG) using the different models is also shown
 750 (Fig. 7c).

751
 752 At 800°C , the G – P curves of glass-like carbon (pre-
 753 ferred model) and of graphite cross at 3.4 GPa, showing a
 754 continuous decline of ΔG with increasing pressure, which
 755 is 1.5 kJ/mol at 1 GPa and 0.29 kJ/mol at 3 GPa. These
 756 ΔG values match well our experimental results at $f\text{H}_2^{\text{NNO}}$
 757 conditions (Table 3). Runs buffered at $f\text{H}_2^{\text{FMQ}}$ conditions
 758 agree with the model at 1 GPa, while at 3 GPa the decline
 759 observed experimentally, characterized by a negative ΔG , is
 760 more pronounced compared to the model. Models assum-
 761 ing a molar volume coherent with the apparent bulk density
 762 of glass-like carbon (1.5 g/cm^3) are inconsistent with exper-
 763 imental results, as they show ΔG values that would increase
 764 by increasing pressures (red dashed line in Fig. 7). Negative
 765 ΔG values at 3 GPa can be reproduced only by models that
 766 assume very high compressibility ($K^0 = 2$ GPa; orange
 767 dashed line in Fig. 7). In this case, however, the intersection
 768 point with graphite is shifted at lower pressures (≈ 1.5 GPa),
 769 so that the G – P curve of glass-like carbon would always lie
 770 below that of diamond, meaning that, above the intersec-
 771 tion point, glass-like carbon would be the stable form of
 772 carbon relative graphite and diamond, which is unlikely.
 773 On the other hand, the preferred model does intersect the
 774 G – P curve of diamond, although it occurs at 4.2 GPa,
 775 i.e., above the intersection point with graphite at 3.4 GPa
 776 and above the graphite–diamond transition at 3.7 GPa,
 777 too. This would imply that in the pressure window 3.4–
 778 3.7 glass-like carbon could be more stable than graphite
 779 and between 3.7 and 4.2 it could even be more stable than
 780 diamond (yellow field in Fig. 7). However, because of the
 781 similar slopes of glass-like carbon- and graphite G – P
 782 curves, small fluctuations in the chosen K^0 can result in
 783 large uncertainties on the position of the intersection point
 784 with graphite relative to the graphite–diamond transition.
 785 In fact, a glass-like carbon G – P curve calculated assum-
 786 ing $K^0 = 12$ GPa (red dashed lines in Fig. 7) instead of
 787 $K^0 = 9$ GPa (preferred model) would intersect the G – P
 788 curve of diamond at 3.4 GPa and the G – P curve of graph-
 789 ite at 4 GPa, implying metastability of glass-like carbon at any



pressure towards both graphite and diamond, without having a marked effect on the predicted decline of ΔG with increasing pressure.

The estimated thermodynamic parameters of glass-like carbon allow also the calculation of fO_2 – T phase diagrams at high pressures. In Fig. 8, the boundaries C–CO₂ (often referred to as CCO) and enstatite + magnesite = olivine + C (EMOG) are compared considering crystalline graphite and glass-like carbon. At 1 GPa, CCO_(glass-like carbon) and EMOG_(glass-like carbon) are shifted below CCO_(graphite) and EMOG_(graphite) by 0.08 log fO_2 units. At 3.5 GPa, the possible reversed stability of glass-like carbon over graphite is shown, with CCO_(glass-like carbon) and EMOG_(glass-like carbon) located above CCO_(graphite) and EMOG_(graphite) by 0.01 log fO_2 units. In both cases, the difference of CCO curves pertaining to the two considered types of carbon is very small in terms of absolute fO_2 values. Nevertheless, as shown by our experimental results, these differences are enough to induce large variations in the composition of COH fluids interacting with crystalline versus glass-like solid carbon.

4.4. Comparison of glass-like carbon and glucose-derived char

Char synthesized for 24 h at 1 and 3 GPa, 800 °C starting from glucose displays conchoidal fractures (Fig. 3c–f) and absence of cleavage, similar to glass-like carbon. Moreover, char and glass-like carbon show broadly similar Raman spectra (Fig. 4), X-ray diffraction patterns (Supplementary Fig. 3) and nano-sized crystallite dimensions, supporting our experimental strategy in which glass-like carbon was chosen as the best analogue for disorganized, poorly crystalline carbonaceous organic matter. In this study, we observed a marked difference in Raman spectra acquired for char synthesized in 12-h and 24-h runs performed at 1 GPa and 800 °C. In particular, the graphite G peak at about 2700 cm⁻¹, well developed in the 12-h run, becomes only hinted in the 24-h run, suggesting that the size of the graphite crystallites decreased with time. This implies, in agreement with Beyssac et al. (2003), that the structure of char, although somewhat similar to glass-like carbon, is not stable at high-pressure/high-temperature conditions, and so this type of materials would be not suitable for long experiments at static equilibrium conditions. In this study, however, we observed transient near-equilibrium conditions between char and aqueous fluids generated by dehydration of glucose. Ideally, in perfectly

closed systems, the thermal decomposition of anhydrous glucose (CH₂O) should produce carbon and pure water; however, this has been observed only in the run performed at 3 GPa and 800 °C, containing almost pure water (≈ 99 mol% H₂O). In fact, dehydration of glucose at 1 GPa produced CH₄-rich, CO₂-bearing fluids after 12 h and CO₂-rich, CH₄-bearing fluids after 24 h. However, if the measured composition of these fluids is compared with those predicted by the modified model of Zhang and Duan (2009) implemented with the retrieved glass-like carbon equilibrium constants, both XCO_2 and XCH_4 ratios match redox conditions of $\Delta FMQ = -1.8$, suggesting near-equilibrium conditions and a close thermodynamic affinity between glass-like carbon and char. In longer runs (24 h) at the same conditions of 1 GPa and 800 °C, measured XCO_2 and XCH_4 ratios correspond also in this case to consistent redox states ($\Delta FMQ = -1.2$, if XCO_2 is considered; $\Delta FMQ = -1.0$ if XCH_4 is taken into account). The measured fluid compositions suggest that the interaction with char in unbuffered single gold capsules evolves over time from reduced conditions, likely buffered by glucose (Hawkins, 1929; Kunz et al., 2011), to more oxidized conditions, likely constrained by the MgO–graphite–NaCl–Pyrex furnace assembly (close to FMQ; cf. Olafsson and Eggler, 1983). In agreement with previous studies (e.g., Truckenbrodt et al., 1997; Truckenbrodt and Johannes, 1999; Matjuschkina et al., 2014), we observed that unbuffered single gold capsules cannot therefore be considered systems perfectly closed to H₂O and H₂, so the buffering of the system (for instance using double capsules) is mandatory to constrain the H₂ (and, indirectly, the O₂) chemical potential.

4.5. Implications for organic matter dissolution at subduction zones

Organic matter can be an important constituent of oceanic sediments (Mayer et al., 1992), and on average it accounts for less than 1 wt.% (Kelemen and Manning, 2015). Nevertheless, organic matter in deep-sea fans can dominate the carbon input flux at some margins (Plank and Manning, 2019). The proportion of organic to inorganic carbon (i.e., marine carbonates) subducted globally is about 20% (Plank and Manning, 2019) and the total amount of organic carbon subducted in modern active subduction zones is estimated > 11 Mt C/y (Clift, 2017). Once subducted and heated, poorly organized organic matter is progressively transformed into crystalline graphite through

Fig. 7. Thermodynamic properties of glass-like carbon. (A) glass-like carbon bulk modulus and its pressure dependence, compared with graphite. Measurements from Zhao et al. (2015) (green dots) are fitted with different K^0 and K' . The preferred model (red thick) assumes $K^0 = 9$ GPa and $K' = 2.9$. See text for other details. (B) Gibbs free energy versus pressure at 800 °C, calculated using different thermodynamic models of glassy carbon. Red arrows indicate the shift of the preferred model assuming either an increased molar volume (i.e., lower density) or an increased compressibility (lower K^0). (C) difference in Gibbs free energy between glass-like carbon and graphite (ΔG), plotted as a function of pressure at $T = 800$ °C. Red thick (preferred model): $K^0 = 9$ GPa, $K' = 2.9$, density (d) = 2.25 g/cm³. Red dashed: $K^0 = 12$ GPa, $K' = 2.9$, $d = 2.25$ g/cm³. Purple dashed: $K^0 = 15$ GPa, $K' = -2.4$, $d = 2.25$ g/cm³. Orange dashed: $K^0 = 0.1$ GPa, $K' = 6.3$, $d = 2.25$ g/cm³. Green dashed: $K^0 = 9$ GPa, $K' = 2.9$, $d = 1.5$ g/cm³. Blue: diamond. Black thick: graphite. Light yellow field: thermodynamic stability of glass-like carbon (preferred model) over graphite and diamond. (For interpretation of the references to colour in this figure legend, the reader is referred to the web version of this article.)

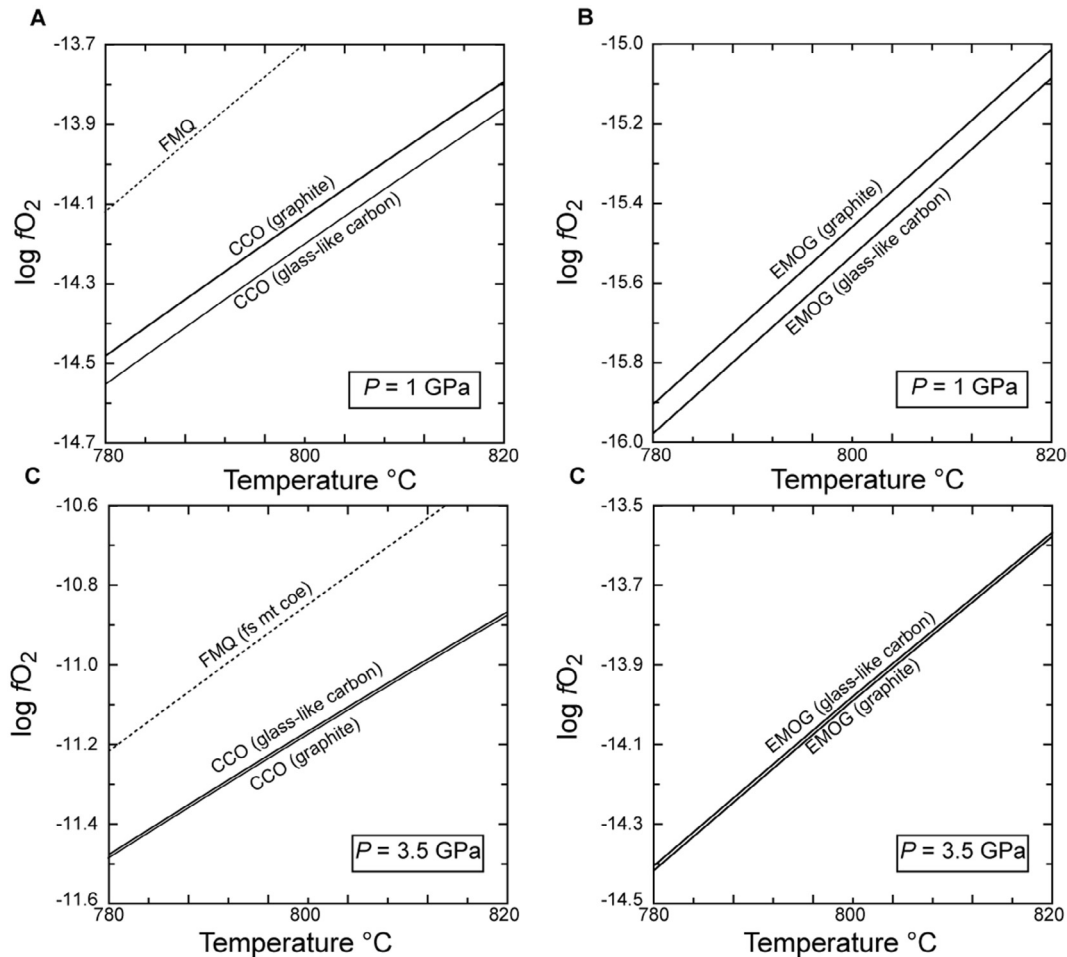


Fig. 8. Calculated T - $\log f_{\text{O}_2}$ diagrams of the univariant equilibria $\text{C} + \text{O}_2 = \text{CO}_2$ (CCO) and $\text{MgSiO}_3 + \text{MgCO}_3 = \text{Mg}_2\text{SiO}_4 + \text{C} + \text{O}_2$ (EMOG) involving graphite and glass-like carbon close to $T = 800^\circ\text{C}$ at $P = 1$ GPa and at $P = 3.5$ GPa, using the thermodynamic properties reported in Table 4. FMQ: fayalite-magnetite-quartz or ferrosilite (fs)-magnetite (mt)-coesite (coes) oxygen buffer.

882 a multitude of intermediate stages generally referred to dis-
 883 ordered graphitic carbon (Beyssac and Rumble, 2014;
 884 Buseck and Beyssac, 2014). In addition, graphite can also
 885 form by reduction of carbonates during subduction
 886 (Galvez et al., 2013; Vitale-Brovarone et al., 2017) and by
 887 precipitation from subduction C-O-H fluids (Luque et al.,
 888 1998).

889 The oxidation susceptibility and therefore the dissolu-
 890 tion of graphite in aqueous fluids varies as a function of
 891 P , T and f_{O_2} conditions (e.g., Connolly, 1995; Tumiati
 892 and Malaspina, 2019). In general, low-temperature and
 893 high-pressure conditions characterizing subduction zones
 894 are thought to promote the stability of graphite, thus fluids
 895 interacting with this mineral should contain very low
 896 amounts of carbon and are essentially nearly pure water
 897 (Schmidt and Poli, 2013). However, we show in Fig. 9a that
 898 this is expected only at forearc conditions. In fact, at P - T
 899 conditions characterizing the slab surface (Syracuse et al.,
 900 2010), nearly pure water is expected only up to around 2
 901 GPa and 450°C . At greater depths, graphite-saturated flu-
 902 ids become progressively more enriched in CO_2 as FMQ
 903 and CCO buffers get very close (Fig. 9a), with maximum

904 CO_2 contents ($X_{\text{CO}_2} = 0.55$) at subarc conditions (3 904
 905 GPa– 700°C), where the two buffers nearly converge. These 905
 906 fluid compositions are predicted assuming a perfectly crys- 906
 907 talline and ordered state of graphite. Several previous stud- 907
 908 ies suggested that the poorly ordered graphite might behave 908
 909 differently, in particular showing a higher solubility in aque- 909
 910 ous fluids (Ziegenbein and Johannes, 1980; Connolly, 1995; 910
 911 Luque et al., 1998). Although our investigated P - T condi- 911
 912 tions are not strictly comparable with “normal” subduction 912
 913 regimes, especially at low pressures, we demonstrate that 913
 914 glass-like carbon is characterized by a marked difference 914
 915 in free energy (≈ 2 kJ/mol) with respect to crystalline gra- 915
 916 phite at low pressures, diminishing with increasing pres- 916
 917 sures and with a possible sign reversal close to graphite- 917
 918 diamond transition (located at 3.6 GPa and 760°C in 918
 919 Fig. 9a). Because we showed that the difference in free 919
 920 energy between graphite and glass-like carbon is predomi- 920
 921 nantly due to their different compressibility behavior, the 921
 922 relative difference in carbon solubility is only slightly 922
 923 depending on temperature. Therefore, we can speculate that 923
 924 similar differences in fluid carbon content (in terms of CO_2 924
 925 (aq), but possibly also of $\text{CH}_{4(\text{aq})}$, HCO_3^{3-} , CO_3^{2-} and other 925

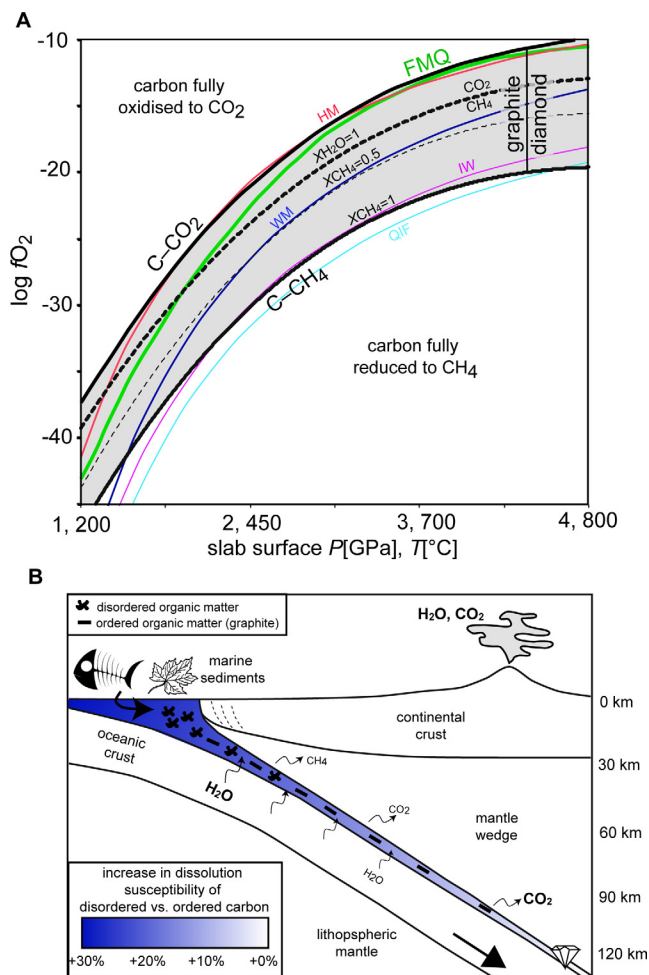


Fig. 9. Fate of organic matter in subduction. (A) Stability of COH fluids (grey field) calculated as a function of fO_2 along a subduction P – T gradient consistent with the average thermal model of slab surface after Syracuse et al. (2010). COH fluids are stable between the two boundaries $C + O_2 = CO_2$ (CCO) and $C + 2 H_2 = CH_4$. At this scale, differences between graphite and amorphous carbon are negligible, but according to the preferred model in Fig. 7 glass-like carbon would be the stable carbon polymorph at $P > 3.4$ GPa. The calculation of fluid isopleths ($XCO_2 = CO_2/H_2O + CO_2$; $XCH_4 = CH_4/H_2O + CH_4$) has been performed using the Perple_X and the EoS of Connolly and Cesare (1993). Reference buffers FMQ, hematite–magnetite (HM), wustite–magnetite (WM), iron–wustite (IW) and quartz–iron–fayalite (QIF) are shown for reference. Fluids in equilibrium with graphite buffered at FMQ conditions become increasingly enriched in CO_2 , which reaches its maximum concentration at about 100 km depth, where FMQ and CCO almost converge. (B) Cartoon showing the fate of organic matter in subduction zones. Disordered organic matter contained in marine sediments undergoes partial to complete graphitization by increasing subduction temperature. Experimental results and thermodynamic models presented in this study indicate that disordered carbon is more prone to oxidation with respect to crystalline carbon especially at low pressures, characterizing the forearc region. At these depths, an intense flush of water would be able to dissolve selectively disordered organic matter from the subducted sediments, while graphite behaves in a more refractory manner. This differential dissolution susceptibility is expected to progressively decrease as subduction proceeds, vanishing at about 100 km depth where the difference in free energy between graphite and disordered carbon tends to zero.

926 dissolved C–O–H species at appropriate P – T – fO_2 – fH_2 –pH
 927 conditions) can be expected at lower temperatures charac-
 928 terizing the subduction zones and in particular the subduc-
 929 tion surface where sediments containing organic matter can
 930 be abundant.

931 This implies that disordered graphitic carbon is more
 932 prone to oxidation if compared with ordered crystalline
 933 graphite down to about 110 km, resulting in fluids that
 934 are enriched in CO_2 compared to current estimates: the
 935 lower the pressure the higher the differential dissolution sus-
 936 ceptibility. Therefore, because it is unlikely that organic
 937 carbon can persist in its disordered state at great depths

and consequent relatively high temperatures (Beysnac 938
 et al., 2002), and because the difference in free energy is 939
 higher at low pressures, we infer that the most important 940
 effect on carbon recycling concerns the most shallow levels 941
 of subduction zones, where disordered organic carbon 942
 could be far more reactive than expected for graphite 943
 towards aqueous fluids (Fig. 9b). 944

Obviously an important source of uncertainty arises 945
 from the assumption that glass-like carbon can be consid- 946
 ered an analogue of disordered natural carbonaceous mat- 947
 ter. Carbon materials are very complex because their 948
 properties change extensively with structural defects and 949

950 impurities, and the type of hybridization, in particular sp^2
 951 (graphite-like carbon) vs. sp^3 (diamond-like carbon) (e.g.,
 952 Robertson, 2002; Langenhorst and Campione, 2019).
 953 Moreover, the activity and the reactivity of these materials
 954 can be modified by bringing them to nanosize dimensions.
 955 For instance, Guencheva et al. (2001) and Gutzow et al.
 956 (2005) showed that nanodispersed (10 nm) glass-like carbon
 957 displays a difference in Gibbs free energy compared to gra-
 958 phite of +12 kJ/mol at standard conditions, which is sub-
 959 stantially higher relative to bulk glass-like carbon
 960 (+2.4 kJ/mol; Table 4) and which would result in dissolu-
 961 tion susceptibility higher than that provided in our study.
 962 In addition, natural highly disordered carbon, as synthetic
 963 amorphous and graphitic carbon, is likely characterized
 964 by a higher kinetic reactivity because of the presence of
 965 active immobilized free radicals (dangling bonds) and
 966 defects which make these materials efficient catalysts (e.g.,
 967 Jüntgen, 1986). The results provided in our study therefore
 968 represent a first attempt to provide a conservative minimum
 969 estimate of the enhanced dissolution of disordered carbon
 970 with respect to crystalline graphite in natural systems.

971 5. CONCLUSIONS

972 Well-ordered crystalline graphite and X-ray amorphous
 973 glass-like carbon display different dissolution susceptibility
 974 in aqueous fluids, because of their different thermodynamic
 975 properties. On the basis of our experimental observations
 976 concerning this type of disordered sp^2 carbon, and aware
 977 of the uncertainties arising from the choice of glass-like car-
 978 bon as an analogue materials for naturally occurring poorly
 979 organized carbon derived from the graphitization of
 980 organic matter, we may speculate at this stage that also nat-
 981 ural poorly organized graphitic carbon could behave in a
 982 different manner compared to perfectly crystalline graphite.
 983 In particular, disordered carbonaceous matter could be
 984 more prone to dissolve in aqueous fluids compared to
 985 well-crystallized graphite especially at pressures corre-
 986 sponding to the forearc region of subduction zones. High
 987 fluxes of water coming from the dehydration of the
 988 down-going slab would therefore induce an effective
 989 removal of organic matter from its sedimentary cover,
 990 prompting metasomatism of the mantle wedge (Sieber
 991 et al., 2018) and contributing to the global deep carbon
 992 cycle. As for glass-like carbon, the differential dissolution
 993 susceptibility declines with increasing pressure correspond-
 994 ing to 110 km depth, below which “disordered” carbon
 995 could be even less soluble than graphite. The stability of
 996 glass-like carbon over diamond, although predicted by the
 997 suggested model in the 3.7–4.2 GPa pressure window, relies
 998 on thermodynamic parameters that are affected by uncer-
 999 tainties that are currently unquantifiable. The occurrence
 1000 of nano-crystalline disordered graphitic carbon and amor-
 1001 phous sp^2 and sp^3 carbon has been indeed reported in
 1002 micro- and nano-sized diamonds from Cignana Lake in
 1003 the Western Alps (Frezzotti et al., 2014; Frezzotti, 2019)
 1004 and glass-like X-ray amorphous carbon has been obtained
 1005 experimentally at diamond-stable conditions (7.7 GPa and
 1006 1000 °C; Yamaoka et al., 2002). However, more investiga-
 1007 tions are required to confirm this hypothesis.

Declaration of Competing Interest

The authors declared that there is no conflict of interest.

ACKNOWLEDGEMENTS

Luca Toffolo is acknowledged for preliminary Raman
 analyses, Andrea Risplendente for help at the microprobe,
 and Andrea Amalfa for preparing some of the experiments.
 Alberto Villa is thanked for helpful discussions about syn-
 thetic carbon forms. Elettra is acknowledged for syn-
 chrotron beamtime. Maurizio Polentarutti and Marco
 Merlini for help at the synchrotron. The authors are
 indebted to the reviewers Yuan Li and Matt Steele-
 MacInnis for their useful suggestions. Suggestions by the
 Associate Editor Rajdeep Dasgupta also contributed to a
 significant improvement of the paper.

FUNDING

ST and SP acknowledge support from Deep Carbon
 Observatory - Sloan Foundation and from Italian program
 MIUR PRIN 2017ZE49E7_002. AVB acknowledges fund-
 ing from the Agence Nationale des Recherches (ANR;
 grant T-ERC), France, and from the Levi Montalcini pro-
 gram by MIUR, Italy. CEM acknowledges support from
 US National Science Foundation grant EAR 1732256.

APPENDIX A. TERMINOLOGY USED FOR THE DESCRIPTION OF SOLID CARBON

In this study, the terminology used for the description of
 solid carbon follows the recommendations of IUPAC
 (Fitzer et al., 1995).

- Graphite: an allotropic form of the element carbon con-
 sisting of layers of hexagonally arranged carbon atoms
 in a planar condensed ring system (graphene layers).
 The layers are stacked parallel to each other in a
 three-dimensional crystalline long-range order. The
 chemical bonds within the layers are covalent with sp^2
 hybridization.
- Graphitic carbon: all varieties of substances consisting
 of the element carbon in the allotropic form of graphite
 irrespective of the presence of structural defects. The use
 of the term is justified if three-dimensional hexagonal
 long-range order can be detected in the material by
 diffraction methods, independent of the volume fraction
 and the homogeneity of distribution of such crystalline
 domains.
- Glass-like carbon: in this study we use this term
 although the commercial/trademark terms “glassy car-
 bon” and “vitreous carbon” are still widely used in
 experimental petrology and materials sciences papers.
 Glass-like carbon is agranular (i.e., homogenous
 microstructure with structural elements undistinguish-
 able by optical microscopy) and non-graphitizable car-
 bon (i.e., it does not convert into graphitic carbon
 upon heat treatment to 2500–3300 K) with a very high

isotropy. Although its structure is not comparable to silicate glasses, the fracture surfaces have a pseudo-glassy (conchoidal) appearance. It consists of curved two-dimensional structural elements (graphene layers, i.e., single carbon layers of the graphite structure) dispersed in an X-ray amorphous matrix, but it does not exhibit dangling bonds that characterize the so-called “amorphous carbon”. In fact, the term “amorphous carbon” is restricted to the description of carbon materials which, in addition to a lack of long-range crystalline order and to deviations of the interatomic distances with respect to graphite lattice as well as to the diamond lattice, show deviations in the bond angles because of the presence of dangling bonds. Amorphous carbon is disordered even on the atomic scale and have a fraction of sp^3 bonds ranging from a few (“graphite-like” structure) to almost 100% (“diamond-like” structure) (Sundqvist and Olabi, 2016)

- Char: a solid decomposition product of a natural or synthetic organic material. In this study, char is produced by carbonization (pyrolysis) of glucose. The term pyrolytic carbon has been avoided because it is restricted to carbon materials deposited from gaseous hydrocarbon compounds by chemical vapor deposition.

APPENDIX B. SUPPLEMENTARY MATERIAL

Supplementary data to this article can be found online at <https://doi.org/10.1016/j.gca.2020.01.030>.

REFERENCES

Bernard S., Benzerara K., Beyssac O., Menguy N., Guyot F., Brown G. E. and Goffé B. (2007) Exceptional preservation of fossil plant spores in high-pressure metamorphic rocks. *Earth Planet. Sci. Lett.* **262**, 257–272.

Beyssac O., Brunet F., Petitot J.-P., Goffé B. and Rouzaud J.-N. (2003) Experimental study of the microtextural and structural transformations of carbonaceous materials under pressure and temperature Available at: *Eur. J. Mineral.* **15**, 937–951 <http://www.ingentaselect.com/rpsv/cgi-bin/cgi?ini=xref&body=linker&reqdoi=10.1127/0935-1221/2003/0015-0937>.

Beyssac O., Rouzaud J.-N., Goffé B., Brunet F. and Chopin C. (2002) Graphitization in a high-pressure, low-temperature metamorphic gradient: a Raman microspectroscopy and HRTEM study Available at: *Contrib. Mineral. Petrol.* **143**, 19–31 <http://link.springer.com/10.1007/s00410-001-0324-7>.

Beyssac O. and Rumble D. (2014) Graphitic carbon: a ubiquitous, diverse, and useful geomaterial. *Elements* **10**, 415–420.

Bollinger L., Avouac J. P., Beyssac O., Catlos E. J., Harrison T. M., Grove M., Goffé B. and Sapkota S. (2004) Thermal structure and exhumation history of the Lesser Himalaya in central Nepal. *Tectonics* **23**, 1–19.

Bose K. and Ganguly J. (1995) Quartz-coesite transition revisited - Reversed experimental determi at 500–1200 °C and retrieved thermochemical properties. *Am. Mineral. Mineral.* **80**, 231–238.

Buseck P. R. and Beyssac O. (2014) From organic matter to graphite: graphitization. *Elements* **10**, 421–426.

Cappelletti R. L., Udovic T. J. and Paul R. L. (2018) Glassy carbon, NIST Standard Reference Material (SRM 3600): hydrogen content, neutron vibrational density of states and heat capacity. *J. Appl. Crystallogr.* **51**, 1323–1328.

Cartigny P., Stachel T., Harris J. W. and Javoy M. (2004) Constraining diamond metasomatic growth using C- and N-stable isotopes: examples from Namibia. *Lithos* **77**, 359–373.

Clift P. D. (2017) A revised budget for Cenozoic sedimentary carbon subduction. *Rev. Geophys.* **55**, 97–125.

Connolly J. A. D. (2005) Computation of phase equilibria by linear programming: a tool for geodynamic modeling and its application to subduction zone decarbonation. *Earth Planet. Sci. Lett.* **236**, 524–541.

Connolly J. A. D. (1995) Phase diagram methods for graphitic rocks and application to the system. *Contrib. Mineral. Petrol.*, 94–116.

Connolly J. A. D. and Cesare B. (1993) C-O-H-S fluid composition and oxygen fugacity in graphitic metapelites. *J. Metamorph. Geol.* **11**, 379–388.

Cowland F. C. and Lewis J. C. (1967) Vitreous carbon – a new form of carbon. *J. Mater. Sci.* **2**, 507–512.

Dasgupta R., Hirschmann M. M. and Dellas N. (2005) The effect of bulk composition on the solidus of carbonated eclogite from partial melting experiments at 3 GPa. *Contrib. Mineral. Petrol.* **149**, 288–305.

Day H. W. (2012) A revised diamond-graphite transition curve. *Am. Mineral.* **97**, 52–62.

Duncan M. S. and Dasgupta R. (2017) Rise of Earth’s atmospheric oxygen controlled by efficient subduction of organic carbon. *Nat. Geosci.* **10**, 387–392.

Eugster H. P. and Skippen G. B. (1967) Igneous and metamorphic reactions involving gas equilibria. *Res. Geochem.* **2**, 492–520.

Falloon T. J., Green D. H., Danyushevsky L. V. and McNeill A. W. (2008) The composition of near-solidus partial melts of fertile peridotite at 1 and 1.5 GPa: Implications for the petrogenesis of MORB. *J. Petrol.* **49**, 591–613.

Ferrari A. C. (2007) Raman spectroscopy of graphene and graphite: disorder, electron-phonon coupling, doping and nonadiabatic effects. *Solid State Commun.* **143**, 47–57.

Ferrari A. C. and Robertson J. (2001) Resonant Raman spectroscopy of disordered, amorphous, and diamond-like carbon. *Phys. Rev. B* **64**, 075414.

Fitzer E., Köchling K. H., Boehm H. P. and Marsh H. (1995) Recommended terminology for the description of carbon as a solid. *Pure Appl. Chem.* **67**, 473–506.

Frezzotti M. L. (2019) Diamond growth from organic compounds in hydrous fluids deep within the Earth. *Nat. Commun.* **10**. <https://doi.org/10.1038/s41467-019-12984-y>.

Galvez M. E., Beyssac O., Martinez I., Benzerara K., Chaduteau C., Malvoisin B. and Malavieille J. (2013) Graphite formation by carbonate reduction during subduction. *Nat. Geosci.* **6**, 473–477. <https://doi.org/10.1038/ngeo1827>.

Guencheva V., Grantscharova E. and Gutzow I. (2001) Thermodynamic properties of the amorphous and crystalline modifications of carbon and the metastable synthesis of diamond. *Cryst. Res. Technol.* **36**, 1411–1428.

Gutzow I., Todorova S., Kostadinov L., Stoyanov E., Guencheva V., Völksch G., Dunken H. and Rüssel C. (2005) Diamonds by transport reactions with vitreous carbon and from the plasma torch: new and old methods of metastable diamond syhtnesis and growth. In *Nucleation theory and applications* (eds. J. W. P. Schmelzer and J. W. P. Schmelzer). Wiley-VCH Verlag, pp. 256–311.

Hawkins J. A. (1929) Reducing powers of different sugars for the ferriyanide reagent used in the gasometric sugar method. *J. Biol. Chem.* **84**, 79–83.

Hayes J. M. and Waldbauer J. R. (2006) The carbon cycle and associated redox processes through time. *Philos. Trans. R. Soc. Lond. B. Biol. Sci.* **361**, 931–950.

- 1184 Holland T. J. B. and Powell R. (1998) An internally consistent
1185 thermodynamic data set for phases of petrological interest. *J.*
1186 *Metamorph. Geol.* **16**, 309–343.
- 1187 Hu M., He J., Zhao Z., Strobel T. A., Hu W., Yu D., Sun H., Liu
1188 L., Li Z., Ma M., Kono Y., Shu J., Mao H., Fei Y., Shen G.,
1189 Wang Y., Juhl S. J., Huang J. Y., Liu Z., Xu B. and Tian Y.
1190 (2017) Compressed glassy carbon: an ultrastrong and elastic
1191 interpenetrating graphene network. *Sci. Adv.* **3**, e1603213.
- 1192 Huang F., Daniel L., Cardon H., Montagnac G. and Sverjensky D.
1193 A. (2017) Immiscible hydrocarbon fluids in the deep carbon
1194 cycle. *Nat. Commun.* **8**, 15798.
- 1195 Huang F. and Sverjensky D. A. (2019) Extended Deep Earth Water
1196 Model for predicting major element mantle metasomatism.
1197 *Geochim. Cosmochim. Acta* **254**, 192–230. <https://doi.org/10.1016/j.gca.2019.03.027>.
- 1198 Jüntgen H. (1986) Activated carbon as catalyst support. A review
1199 of new research results. *Fuel* **65**, 1436–1446.
- 1200 Kelemen P. B. and Manning C. E. (2015) Reevaluating carbon
1201 fluxes in subduction zones, what goes down, mostly comes up
1202 201507889. *Proc. Natl. Acad. Sci.* <http://www.pnas.org/lookup/doi/10.1073/pnas.1507889112>.
- 1203 Kunz T., Lee E. J., Schiwiek V., Seewald T. and Methner F. J.
1204 (2011) Glucose – a reducing sugar? Reducing properties of
1205 sugars in beverages and food. *Brew. Sci.* **64**, 61–67.
- 1206 Langenhorst F. and Campione M. (2019) Ideal and real structures
1207 of different forms of carbon, with some remarks on their
1208 geological significance. *J. Geol. Soc. Lond.* **176**, 337–347.
- 1209 Li Y. (2016) T1 - Immiscible C-H-O fluids formed at subduction
1210 zone conditions. *Geochem. Perspect. Lett.* **3**, 12–21 <http://www.geochemicalperspectivesletters.org/article1702>.
- 1211 Luque F. J., Pasteris J. D., Wopenka B., Rodas M. and
1212 Barrenechea J. F. (1998) Natural fluid-deposited graphite:
1213 Mineralogical characteristics and mechanisms of formation.
1214 *Am. J. Sci.* **298**, 471–498.
- 1215 Luth R. W. (1989) Natural versus experimental control of
1216 oxidation state : Effects on the composition and speciation of
1217 C-O-H fluids. *Am. Mineral.* **74**, 50–57.
- 1218 Manning C. E., Shock E. L. and Sverjensky D. A. (2013) The
1219 chemistry of carbon in aqueous fluids at crustal and upper-
1220 mantle conditions: experimental and theoretical constraints
1221 (accessed April 5, 2019). *Rev. Mineral. Geochemistry* **75**, 109–
1222 148 <https://pubs.geoscienceworld.org/rimg/article/75/1/109-148/140933>.
- 1223 Mason E., Edmonds M. and Turchyn A. V. (2017) Remobilization
1224 of crustal carbon may dominate volcanic arc emissions. *Science*
1225 (80-) **357**, 290–294.
- 1226 Matjuschkin V., Brooker R. A., Tattitch B., Blundy J. D. and
1227 Stamper C. C. (2014) Control and monitoring of oxygen
1228 fugacity in piston cylinder experiments. *Contrib. Mineral.*
1229 *Petrol.* **169**, 1–16.
- 1230 Mattioli G. S. and Wood B. J. (1988) Magnetite activities across
1231 the MgAl₂O₄-Fe₃O₄ spinel join, with application to thermo-
1232 barometric estimates of upper mantle oxygen fugacity. *Contrib.*
1233 *Mineral. Petrol.* **98**, 148–162.
- 1234 Matveev S., Ballhaus C., Fricke K., Truckenbrodt J. and Ziegen-
1235 ben D. (1997) Volatiles in the Earth's mantle: I. Synthesis of
1236 CHO fluids at 1273 K and 2.4 GPa. *Geochim. Cosmochim. Acta*
1237 **61**, 3081–3088.
- 1238 Mayer L., Pisiyas N. and Janacek T. (1992) 14. SITE 849. *Proc.*
1239 *Ocean Drill. Program. Initial Rep.* **138**, 735–807.
- 1240 McCollom T. M. (2013) Laboratory simulations of abiotic
1241 hydrocarbon formation in Earth's deep subsurface. *Rev.*
1242 *Mineral. Geochem.* **75**, 467–494. <https://doi.org/10.2138/rmg.2013.75.15>.
- 1243 O'Neill H. S. C. and Pownceby M. I. (1993) Thermodynamic data
1244 from redox reactions at high temperatures. I. An experimental
1245 and theoretical assessment of the electrochemical method using
1246 stabilized zirconia electrolytes, with revised values for the Fe-
1247 "FeO", Co-CoO, Ni-NiO and Cu-Cu₂O oxygen buffers, and
1248 new data for the W-WO₂ buffer. *Contrib. Mineral. Petrol.* **114**,
1249 296–314 <http://link.springer.com/article/10.1007/BF01046533>.
- 1250 Olafsson M. and Eggler D. H. (1983) Phase relations of amphibole,
1251 amphibole-carbonate, and phlogopite-carbonate peridotite:
1252 petrologic constraints on the asthenosphere. *Earth Planet. Sci.*
1253 *Lett.* **64**, 305–315.
- 1254 Palot M., Pearson D. G., Stern R. A., Stachel T. and Harris J. W.
1255 (2014) Isotopic constraints on the nature and circulation of
1256 deep mantle C-H-O-N fluids: carbon and nitrogen systematics
1257 within ultra-deep diamonds from Kankan (Guinea). *Geochim.*
1258 *Cosmochim. Acta* **139**, 26–46. <https://doi.org/10.1016/j.gca.2014.04.027>.
- 1259 Pan D. and Galli G. (2016) The fate of carbon dioxide in water-rich
1260 fluids under extreme conditions. *Sci. Adv.* **2**, e1601278. <https://doi.org/10.1126/sciadv.1601278>.
- 1261 Plank T. and Manning C. E. (2019) Subducting carbon. *Nature*
1262 **574**, 343–352. <https://doi.org/10.1038/s41586-019-1643-z>.
- 1263 Ponschke M. A. and House J. E. (2011) Kinetic studies on the loss
1264 of water from α -D-glucose monohydrate. *Carbohydr. Res.* **346**,
1265 2285–2289. <https://doi.org/10.1016/j.carres.2011.07.012>.
- 1266 Robertson J. (2002) Diamond-like amorphous carbon. *Mater. Sci.*
1267 *Eng. Rep.* **37**, 129–281.
- 1268 Robinson J. A. C., Wood B. J. and Blundy J. D. (1998) The
1269 beginning of melting of fertile and depleted peridotite at 1.5
1270 GPa. *Earth Planet. Sci. Lett.* **155**, 97–111.
- 1271 Schmidt M. W. and Poli S. (2013) Devolatilization during
1272 subduction 2nd ed.. *Treatise Geochemistry* **4**, 669–701. <https://doi.org/10.1016/B978-0-08-095975-7.00321-1>.
- 1273 Shiell T. B., McCulloch D. G., McKenzie D. R., Field M. R.,
1274 Haberl B., Boehler R., Cook B. A., De Tomas C., Suarez-
1275 Martinez I., Marks N. A. and Bradby J. E. (2018) Graphitiza-
1276 tion of glassy carbon after compression at room temperature.
1277 *Phys. Rev. Lett.* **120**, 215701. <https://doi.org/10.1103/PhysRevLett.120.215701>.
- 1278 Sieber M. J., Hermann J. and Yaxley G. M. (2018) An
1279 experimental investigation of C–O–H fluid-driven carbonation
1280 of serpentinites under forearc conditions. *Earth Planet. Sci.*
1281 *Lett.* **496**, 178–188. <https://doi.org/10.1016/j.epsl.2018.05.027>.
- 1282 Spandler C., Yaxley G., Green D. H. and Rosenthal A. (2008)
1283 Phase relations and melting of anhydrous K-bearing eclogite
1284 from 1200 to 1600°C and 3 to 5 GPa. *J. Petrol.* **49**, 771–795.
- 1285 Stachel T., Harris J., Aulbach S. and Deines P. (2002) Kankan
1286 diamonds (Guinea) III: $\delta^{13}\text{C}$ and nitrogen characteristics of
1287 deep diamonds. *Contrib. to Mineral. Petrol.* **142**, 465–475.
- 1288 Sundqvist B. and Olabi A. G. (2016) Fullerenes and hard carbons.
1289 *Ref. Modul. Mater. Sci. Mater. Eng.*
- 1290 Sverjensky D. A., Harrison B. and Azzolini D. (2014a) Water in the
1291 deep Earth: The dielectric constant and the solubilities of quartz
1292 and corundum to 60kb and 1200°C. *Geochim. Cosmochim. Acta*
1293 **129**, 125–145 <http://linkinghub.elsevier.com/retrieve/pii/S0016703713007151>.
- 1294 Sverjensky D. A., Stagno V. and Huang F. (2014b) Important role
1295 for organic carbon in subduction-zone fluids in the deep carbon
1296 cycle. *Nat. Geosci.* **7**, 909–913 <http://www.nature.com/doi/10.1038/ngeo2291>.
- 1297 Syracuse E. M., van Keken P. E., Abers G. a., Suetsugu D., Bina
1298 C., Inoue T., Wiens D. and Jellinek M. (2010) The global range
1299 of subduction zone thermal models. *Phys. Earth Planet. Inter.*
1300 **183**, 73–90.
- 1301 Takahashi Y. and Westrum E. F. J. (1970) Glassy carbon low-
1302 temperature thermodynamic properties. *J. Chem. Thermodyn.* **2**,
1303 847–854.

- 1315 Tiraboschi Carl, Tumiati S., Recchia S., Miozzi F. and Poli S. 1346
 1316 (2016) Quantitative analysis of COH fluids synthesized at HP- 1347
 1317 HT conditions: an optimized methodology to measure volatiles 1348
 1318 in experimental capsules. *Geofluids* **16**, 841–855. [https://doi.org/](https://doi.org/10.1111/gfl.12191) 1349
 1319 [10.1111/gfl.12191](https://doi.org/10.1111/gfl.12191). 1350
- 1320 Tiraboschi C., Tumiati S., Sverjensky D., Pettke T., Ulmer P. and 1351
 1321 Poli S. (2018) Experimental determination of magnesia and 1352
 1322 silica solubilities in graphite-saturated and redox-buffered high- 1353
 1323 pressure COH fluids in equilibrium with forsterite + enstatite 1354
 1324 and magnesite + enstatite. *Contrib. Mineral. Petrol.* **173**, 2 1355
 1325 <http://link.springer.com/10.1007/s00410-017-1427-0>. 1356
- 1326 Truckenbrodt J. and Johannes W. (1999) H₂O loss during piston- 1357
 1327 cylinder experiments. *Am. Mineral.* **84**, 1333–1335. 1358
- 1328 Truckenbrodt J., Ziegenbein D. and Johannes W. (1997) Redox 1359
 1329 conditions in piston cylinder apparatus: the different behavior 1360
 1330 of boron nitride and unfired pyrophyllite assemblies. *Am.* 1361
 1331 *Mineral.* **82**, 337–344. 1362
- 1332 Tumiati S. and Malaspina N. (2019) Redox processes and the role 1363
 1333 of carbon-bearing volatiles from the slab–mantle interface to 1364
 1334 the mantle wedge. *J. Geol. Soc. London.* **176**, 388–397. [https://](https://doi.org/10.1144/jgs2018-046) 1365
 1335 doi.org/10.1144/jgs2018-046. 1366
- 1336 Tumiati S., Tiraboschi C., Sverjensky D. A., Pettke T., Recchia S., 1367
 1337 Ulmer P., Miozzi F. and Poli S. (2017) Silicate dissolution 1368
 1338 boosts the CO₂ concentrations in subduction fluids. *Nat.* 1369
 1339 *Commun.* **8**, 616. 1370
- 1340 Vitale Brovarone A., Martinez I., Elmaleh A., Compagnoni R., 1371
 1341 Chaduteau C., Ferraris C. and Esteve I. (2017) Massive 1372
 1342 production of abiotic methane during subduction evidenced in 1373
 1343 metamorphosed ophicarbonates from the Italian Alps. *Nat.* 1374
 1344 *Commun.* **8**, 14134 [http://www.nature.com/doi/10.1038/](http://www.nature.com/doi/10.1038/ncomms14134) 1375
 1345 [ncomms14134](http://www.nature.com/doi/10.1038/ncomms14134).
- Wasylenki L. E. (2003) Near-solidus melting of the shallow upper 1346
 mantle: partial melting experiments on depleted peridotite. *J.* 1347
Petrol. **44**, 1163–1191. 1348
- Yokoyama J., Murabayashi M., Takahashi Y. and Mukaibo T. 1349
 (1971) Measurement of high-temperature thermal properties of 1350
 glassy carbon by laser flash method. *TANSO*, 44–47 (accessed 1351
 January 29, 2019) (in Japanese). 1352
- Zhang C. and Duan Z. (2009) A model for C-O-H fluid in the 1353
 Earth's mantle. *Geochim. Cosmochim. Acta* **73**, 2089–2102. 1354
<https://doi.org/10.1016/j.gca.2009.01.021>. 1355
- Zhang C. and Duan Z. (2010) GFluid: An Excel spreadsheet for 1356
 investigating C-O-H fluid composition under high tempera- 1357
 tures and pressures. *Comput. Geosci.* **36**, 569–572 [http://](http://linkinghub.elsevier.com/retrieve/pii/S0098300409002751) 1358
linkinghub.elsevier.com/retrieve/pii/S0098300409002751. 1359
- Zhang S., Ague J. J. and Vitale Brovarone A. (2018) Degassing of 1360
 organic carbon during regional metamorphism of pelites, 1361
 Wepawaug Schist, Connecticut, USA. *Chem. Geol.* **490**, 30– 1362
 44. <https://doi.org/10.1016/j.chemgeo.2018.05.003>. 1363
- Zhao Z., Wang E. F., Yan H., Kono Y., Wen B., Bai L., Shi F., 1364
 Zhang J., Kenney-Benson C., Park C., Wang Y. and Shen G. 1365
 (2015) Nanoarchitected materials composed of fullerene-like 1366
 spheroids and disordered graphene layers with tunable mechan- 1367
 ical properties. *Nat. Commun.* **6**, 1–10. [https://doi.org/10.1038/](https://doi.org/10.1038/ncomms7212) 1368
[ncomms7212](https://doi.org/10.1038/ncomms7212). 1369
- Ziegenbein D. and Johannes W. (1980) Graphite in C-H-O fluids: 1370
 an unsuitable compound to buffer fluid composition at 1371
 temperatures up to 700°C. *Neues Jahrb. fur Mineral. Monat-* 1372
shefte **7**, 289–305. 1373
 1374

Associate editor: Rajdeep Dasgupta